LBNL-47973

ERNEST ORLANDO LAWRENCE
BERKELEY NATIONAL LABORATORY

High Pressure, High Temperature Scanning Tunneling Microscopy Studies of CO, NO and O_2 on Pt(111) and Rh(111)

Keith B. Rider

Materials Sciences Division
Center for Advanced Materials

May 2001

Ph.D. Thesis

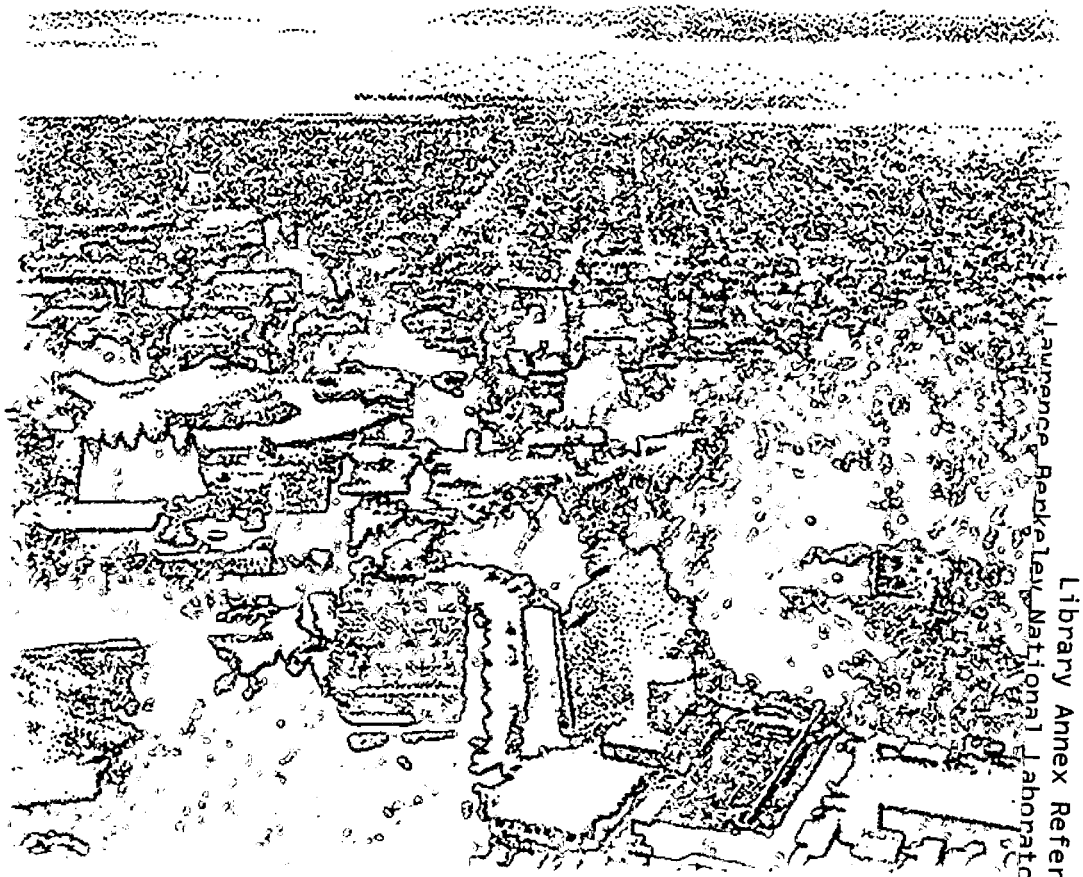

DISCLAIMER

LBNL-47973

High Pressure, High Temperature Scanning Tunneling Microscopy Studies of CO, NO and O_2 on Pt(111) and Rh(111)

Keith Benton Rider
Ph.D. Thesis

Department of Chemistry
University of California, Berkeley

and

Materials Sciences Division
Center for Advanced Materials
Ernest Orlando Lawrence Berkeley National Laboratory
University of California
Berkeley, CA 94720

May 2001

This work was supported by the Director, Office of Science, Office of Basic Energy Sciences, Materials Sciences Division, of the U.S. Department of Energy under Contract No. DE-AC03-76SF00098.

High Pressure, High Temperature Scanning Tunneling Microscopy Studies of CO, NO and O_2 on Pt(111) and Rh(111)

by

Keith Benton Rider

B. S. (Guilford College) 1996

A thesis submitted in partial satisfaction of the

requirements for the degree of

Doctor of Philosophy

in

Chemistry

in the

GRADUATE DIVISION

of the

UNIVERSITY OF CALIFORNIA, BERKELEY

Committee in charge:

Professor Gabor A. Somorjai, Chair

Professor Norman Phillips

Professor Alex Zettl

Spring 2001

High Pressure, High Temperature Scanning Tunneling Microscopy Studies of CO, NO and O_2 on Pt(111) and Rh(111)

by

Keith Benton Rider

Abstract

High Pressure, High Temperature Scanning Tunneling Microscopy

Studies of CO, NO and O_2 on Pt(111) and Rh(111)

by

Keith Benton Rider

Doctor of Philosophy in Chemistry

University of California, Berkeley

Professor Gabor A. Somorjai, Chair

The Scanning Tunneling Microscope (STM) is one of a small number of surface science techniques that can operate at pressures above 10^{-4} Torr. This thesis describes the design of a novel, high-pressure, high-temperature scanning tunneling microscope (HPHTSTM) system and documents its use in examining gas-surface interfaces. A new structure, due to an incommensurate hexagonal overlayer, was observed for CO on the Pt(111) surface in the 200-750 Torr pressure range. This structure has not been observed before at similar coverage under low pressure and temperature conditions.

The adsorption of CO on Rh(111) was studied using a combination of low-pressure and high-pressure STM. The new structures observed at low pressure (10^{-8} to 10^{-6} Torr) included a (2×1) structure and two $(\sqrt{7} \times \sqrt{7})$ R19° structures; the highest coverage

structure, (2 × 2)-3CO, was found to be stable under CO pressures of at least 700 Torr and temperatures up to 80 °C.

NO on Rh(111) was found to form a new (3 × 3) structure in equilibrium with the gas phase near room temperature and at pressures in the Torr range. Two dense adsorbate phases formed, with (2 × 2) and (3 × 3) periodicity. Regions of the surface transformed from one phase to the other as the pressure and temperature changed around the equilibrium *P-T* boundary line. The heat of adsorption of the previously unknown (3 × 3) structure was determined by measuring the pressures and temperatures of coexistence.

The high pressure coadsorption of NO and CO on Rh(111) was also studied with HPHTSTM. For low NO partial pressures, the NO molecules mixed into the (2 × 2)-3CO structure, replacing the CO molecules without changing the symmetry of the adsorbate layer. NO molecules appeared to exhibit a slight preference for sitting on adjacent top-sites in the (2 × 2) lattice, which caused the formation of NO-rich islands at higher NO partial pressures. The presence of CO in the gas phase prevented the formation of the NO (3 × 3) structure until the NO partial pressure was three to five times greater than the CO partial pressure. When the (3 × 3) structure formed, it nucleated on the NO-rich areas.

Dedicated to my parents, Rachel and David Rider, and especially to Rebecca.

Table of Contents

List of Figures

Acknowledgements

Very few people have the opportunity to do research at the cutting edge of science; even fewer are given the freedom to take their research in any direction they please; I had both. I am sincerely grateful to my advisors, Professor Gabor Somorjai and Dr. Miquel Salmeron, for giving me opportunity and freedom, for their patience and for their guidance.

I would also like to thank the past and present members of the Somorjai group with whom I have collaborated. John Jensen assembled the STM apparatus that I used for all of the experiments described in this thesis. If he saw the instrument now, he would find that it is largely unchanged, which is a tribute to his careful design and flawless workmanship. Yong Chen and I worked together on several projects, including the first high-pressure experiments done on the rhodium surface. Kevin Hwang worked on many of the experiments described here. He is a thorough experimentalist and the HPHTSTM is going to produce many interesting results in his hands. Other people who deserve special mention because of their help and friendship are Steve Baldelli, Kyle Kung, Aaron Eppler, Joel Roberts, Mark Rose, Enrico Magni, Paul Cernota, Leo Romm, Frank Ogletree, Michel Van Hove, Falco Netzer and David Gracias.

The staff at Lawrence Berkeley National Laboratory and the U. C. Berkeley College of Chemistry was invaluable. Without the help of technically competent people like them, no one could keep an equipment intensive research project like mine on track. I would especially like to thank Chip Flor, Peter Ruegg, James Wu, Jim Severens, Henry Chan and Eric Gravilund.

Finally, I am grateful to my family for their love and support. My father deserves the credit for my interest in science; he likes to understand things and now so do I. My mother told me how proud she was of me every time I spoke to her during my time at Berkeley. My wife, Rebecca, was a constant source of comfort during the five years it took to complete this thesis. In the next few years, I hope that find she finds that it was time well spent. Rebecca, because of her editing skill, is also largely responsible for the readability of this thesis.

1 Introduction

The development of new materials and material-working techniques has historically been the measure of progress for a society. Historians and archeologists recognize the importance of materials when they name an era, like the Iron Age, after the material-working techniques that were developed during that time. What goes unnoticed is that immediately after the discovery or invention of a new material, we discover or invent methods for modifying the surface of that material to improve its properties. For instance, sometime after we developed woodworking techniques, we found that rubbing the wood surface with a smooth bone made it more waterproof and less likely to break, and after we developed pottery techniques, we began to glaze the pottery to change its surface properties. After we developed ways to produce aluminum in bulk, we developed the process of anodization to protect its surface, and when we created synthetic fibers, we then learned how to control their hydrophobicity. The list goes on, but the point is that if the development of a material is the most important development of an era, then the control over the surface of that material is a close second.

Surface physical chemists are interested the chemistry that happens on a surface of a material. That is, they are interested in the how molecules interact with the surface, how molecules at the surface interact with each other, and how the structures that form do so. These are the principles that all of a surface's chemical properties are based on. A physical chemistry study of a surface might be as simple as measuring the contact angle of a liquid droplet on a surface, or it could require a super-bright monochromatic beam of

x-rays from a synchrotron. In either case, the goal is the same: to understand how and why a surface behaves the way it does.

One of the most fascinating and useful applications of surface chemistry is heterogeneous catalysis; in fact, 70% of all chemicals are fabricated using catalysts [1]. A heterogeneous catalyst is one that exists in a different phase than the reactants and products, so its only interaction with the reactants must take place on its surface. Noble metal heterogeneous catalysts are widely used in the petroleum industry for modifying hydrocarbons. The synthesis and refinement of hydrocarbons make up a large part of the chemical industry, and many of the processes involved (hydrogenation, dehydrocyclization, hydrocracking, etc.) are catalytic. The most important heterogeneous catalysis is probably the Haber-Bosch synthesis of ammonia. Modern agriculture is almost completely dependent on fertilizer made from ammonia—the productivity of the world's farms would plummet without it.

The surface physical chemist is interested in temperature and pressure conditions at which a particular catalytic reaction can be carried out, but most importantly, his questions concern the catalyst material itself. He would like to know the composition and structure of the catalytic surface before, during and after the reaction. He is also challenged by problems related to maximum turnover rate, poisoning, promoter effects, selectivity and structural stability.

Determining surface structure and composition before and after a reaction is relatively easy. There are about 70 different surface science techniques available that can be used [2]. Some of the more common techniques are temperature programmed desorption (TPD), which gives the binding energies of molecules, low energy electron diffraction

(LEED), which gives the surface structure, Auger electron spectroscopy (AES), which gives the atomic composition, and electron energy loss spectroscopy (EELS), which is a vibrational spectroscopy. When combined, these techniques can give a very complete picture of a catalytic surface, provided it is stable in vacuum.

All four of the above mentioned techniques require low pressure conditions to operate, so they work well in an instrument equipped with a high pressure reaction cell that can be isolated from the vacuum chamber. Typically, this is done by positioning the sample in the center of a vacuum chamber and using a hydraulic piston to move a tube-shaped reaction cell over the sample. The reaction cell is pressurized with reactant gases, and the sample is heated to the reaction temperature. The products can be monitored using a gas chromatograph (GC) during the reaction, but none of the surface science techniques above can be used under these conditions.

When the reaction is over, the cell is evacuated and opened. At this point, one can use TPD, LEED, AES or EELS to see what remains on the surface, but this still leaves many unanswered questions about what happened during the reaction. This is the famous "pressure gap"; the system of interest is in a high-pressure environment, but our surface science techniques work in a low-pressure environment.

To bridge this gap, physical surface chemistry needs techniques that can be used to get vibrational, compositional or structural information in high-pressure environments. The most promising technique for getting high-pressure vibrational information is currently sum-frequency generation (SFG). Common, linear infrared spectroscopy can be used on surfaces, but the vibrational frequency of the gas phase molecules is often close to the vibrational frequency of the surface molecules. Since the number of gas phase molecules

along the path of the radiation is so great compared to the number of surface molecules, the absorption by the surface is obscured by the gas phase absorption. To some degree, this problem can be overcome by using a simple background subtraction, but as the pressure increases, the gas will eventually absorb so much of the radiation that the experiment will be compromised. SFG is better suited to high-pressure environments because its selection rules disallow signal production in a centrosymetric medium, such as the gas phase. This, combined with the fact that the signal is well outside of the vibrational range of the gas molecules, makes SFG useful for analyzing surfaces in high-pressure environments.

In anything other than hard vacuum, surface compositional analysis is very difficult to do. One possibility in this area is high-pressure x-ray photoelectron spectroscopy (XPS). It is possible to conduct XPS experiments in the Torr pressure range by differentially pumping an electron analyzer, moving it very close to the sample and using a bright beam of x-rays. This method has the added benefit of serendipitously producing a molecular beam of gas sampled from the near-surface region, which can be analyzed for reaction products. When it is fully developed, high pressure XPS will permit great advances in heterogeneous catalysis.

Surface structure at high pressure can be studied by low angle x-ray diffraction, but x-rays scatter poorly from light elements like carbon and oxygen, so it is of limited use in catalysis. Scanning tunneling microscopy (STM) can be used in high-pressure environments and can be used for structural studies. STM has the advantage of being relatively easy to use because it does not require bright x-ray sources or extreme temperatures.

The primary goals of this research project are to develop the STM as a high-pressure technique for use on model catalysts and to apply it to the reactions of the automobile catalytic converter. One of the topics that we propose to address is whether adsorbates form different structures under high-pressure conditions than they do at similar coverages maintained in vacuum by low temperature. We also want to know how close we can come to real reaction conditions of temperature and pressure before the STM stops producing useful information.

This thesis describes experiments performed between 1996 and 2001 on what might be called a second-generation high pressure, high temperature STM (HPHTSTM). Brian McIntyre [3] did the first HPHTSTM experiments, which inspired this work. His apparatus and results are reviewed in Chapter 2, the bulk of which is an introduction to the technique of STM. Chapter 3 is a description of our experimental apparatus.

The first results from this second-generation HPHTSTM were on the Pt(111)/CO system; Chapter 4 describes how high pressure carbon monoxide forms a previously undiscovered structure on the surface of Pt(111). The formation of this new structure can be completely reversed by reducing the pressure, indicating that it depends on the gas-surface equilibrium to form. Considering that the Pt(111)/CO system is probably the most thoroughly studied of all surface/adsorbate systems, it was encouraging to find new structures so close at hand. Chapter 5 discusses Pt(111) in high pressure oxygen. The results from these studies and the difficulties we had trying to find a tip material compatible with oxygen led us to turn to the CO + NO reaction, which is catalyzed by rhodium. We discovered that CO on Rh(111) at high pressure produces the same structure that has been found at low pressure. This is reported in Chapter 6 and is

interpreted along with results from collaboration with Paul Cernota [4], who worked on low-pressure CO structures on rhodium. Unlike CO, NO on Rh(111) forms a new structure at high pressure. Chapter 7 describes how NO undergoes a phase transition at 0.03 Torr. As with the Pt(111)/CO system, this phase transition is completely reversible by either reducing the pressure or by increasing the temperature, and it only forms when the surface is in equilibrium with the gas phase. We were able to observe this phase transition with the STM as it progressed, yielding very interesting results. Constantly moving closer to reaction conditions, we studied the surface structures of adsorbates on Rh(111) in a mixed gas environment. Chapter 8 details the adsorbate structures on Rh(111) in the mixed CO + NO system. During the course of this work we often saw that the metal atoms on the surface were not immobile as they are in low pressure; instead they were able to move on the surface. Chapter 9 covers metal atom mobility, sometimes due to only the chemistry of the surfaces and sometimes due to the action of the tip. Chapter 10 is a conclusion with comments on future directions of this research.

---

1 K. Christmann, "Introduction to Surface Physical Chemistry," Springer-Verlag, New York (1991).

2 G. A. Somorjai, "Introduction to Surface Chemistry and Catalysis," John Wiley, New York (1994).

3 B.J. McIntyre, M. Salmeron, G.A. Somorjai, *Rev. Sci. Instrum.* **64**, 687 (1993).

4 P. Cernota, K. Rider, H. A. Yoon, M. Salmeron, G. Somorjai, *Surf. Sci.* **445**, 249 (2000).

2 Scanning Tunneling Microscopy (STM)

Binnig and Rohrer built the first scanning tunneling microscope (STM) in 1983 [1, 2]; the importance of their achievement was quickly realized and they were awarded the Nobel Prize for physics in 1986. Scanning tunneling microscopy and other scanning probe techniques are now widely used in surface science. The large number of recent publications that include STM images is the clearest indication of the power of STM. Nearly 20% of the articles published in the journal Surface Science between 1995 and 2001 contain STM images. The scanning tunneling microscope has not replaced any of the traditional experimental techniques of surface science, but has still proved itself useful in a wide variety of situations by allowing real-space, atomic scale imaging of surfaces. Scanning tunneling microscopy was initially used to examine the surfaces of metals, but now can be used for experiments is biology, electrochemistry, surface structure analysis and lithography.

The operation of the STM relies on the quantum mechanical tunneling of electrons. The experimenter prepares atomically sharp metal probe tip and places it a few Angstroms above the surface to be analyzed. When a bias voltage is applied between the tip and sample, electrons tunneling between the tip and sample create a tiny current, which is sensitive to the distance between the tip and sample. As the tip moves over the surface, changes in the tip-surface interaction are recorded in order to create the image. The particular tip-surface interaction that is used to create the image contrast determines the physical meaning of the image.

The following sections contain a description of quantum mechanical tunneling, a discussion of three different contrast mechanisms and a discussion of experimental considerations such as piezoelectric tip positioning and vibration isolation.

2.1 Principle of STM operation – tunneling

As with most topics in physics, the principle of STM is quite simple but treatment of any realistic example becomes devilishly complicated. Consider Fig 2.1, which shows the tip-sample junction of an STM on both the macroscopic and microscopic scale. On the macroscopic scale the tip appears to be infinitely sharp and in direct contact with the sample. On the microscopic scale, though, it is apparent that the tip has a finite radius of curvature and a finite separation from the sample. In the right hand side of Fig. 2.1, the circles represent the atoms; the broken lines indicate the exponentially decreasing equipotential surfaces between the two electrodes. Notice that the distance between the electrodes, the vacuum gap, is only a few atomic diameters. Because the potential decreases so quickly as the electron moves from the vacuum gap toward the electrodes, we often treat the potential as a step function. Under these geometrical conditions the electron wave functions of the two electrodes overlap; when a (slight) potential difference, V_t, is applied the electrons can flow from one electrode to the other. The resulting current density, I_t, depends exponentially on the gap width, d. For the one-dimensional case one can formulate, according to Christmann [3],

$$I_t = \frac{3}{8}\frac{e_0^2}{\hbar}\frac{\chi}{\pi^2 d}V_t e^{-2\chi d}, \qquad 4.1$$

where d is the gap distance in Å, $\chi = \sqrt{2m_0\Phi/\hbar^2}$ and Φ is the average barrier height in eV. Choosing the units of Å and eV makes 2χ approximately equal to $\sqrt{\Phi}$, so if the average barrier height is a few eV, the tunneling current changes by a factor of 10 for every Angstrom of change in *d*. This makes the tunneling current a very sensitive indicator of the tip-sample distance and provides the resolution perpendicular to the surface that is necessary to image individual atoms. The potential diagram in Fig. 2.2 shows the potential that an electron feels as a function of position in the tip, sample or vacuum gap. The potential within either the tip or sample is constant because they are conductors; the potential of the sample relative to the tip is determined by the user-set bias and in the vacuum gap the potential changes linearly. In Fig. 2.2 the tip is shown in the center with a negatively biased sample on the left and a positively biased sample on the right. It is apparent from Eq. 4.1 that there is (other than *d*) another important parameter, Φ, which is the average barrier height or "effective" work function. The barrier height can be approximated as the average of the effective work functions of the tip and sample, $\Phi = \frac{1}{2}(\Phi_t^{eff} + \Phi_s^{eff})$. The effective work functions are not identical to the work functions in a field emission or photoelectric experiment. In STM, the work functions are reduced somewhat due to interactions between the tunneling electrons and the electrons inside the two solids. These interactions can be described classically as image potential effects and lead to a (distance-dependant) reduction of the barrier height. Note that the work function is defined to be the work required to bring an electron from the Fermi level of the solid to a macroscopic distance outside the metal. In the STM

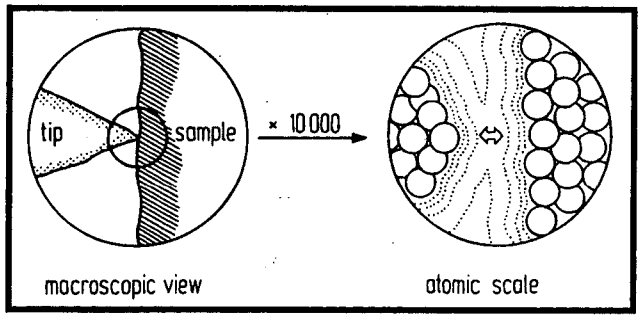

Figure 2.1 Macroscopic and microscopic views of the STM tip-sample junction. The broken lines in the microscopic view are the lines of equipotential. Reproduced from [3].

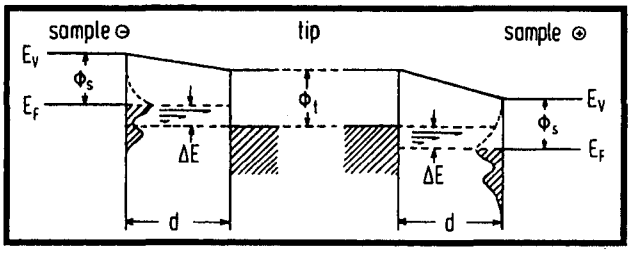

Figure 2.2 Potential diagram of the tunneling junction for two cases. In the first case (left side), the sample is negatively biased and the electrons flow from the filled states of the sample to the empty states of the tip. In the second case (right side), the sample is positively biased and the electrons flow from the filled states of the tip to the empty states of the sample. The shaded areas indicate filled states. Reproduced from [3]. Reproduced from [3].

experiment, however, there are much smaller distances involved, which give rise to perturbations due to the shape of the barrier.

In the preceding section we made no mention of the electronic structure of the electrodes, so let us move beyond the approximations of Eq. 2.1 and return to Fig. 2.2. The figure shows two cases, one in which the sample is biased positive relative to the tip and one where it is biased negative, with the applied bias denoted ΔE. In the first case the electrons flow from the sample to the tip and in the second case the current is reversed. This illustrates the sign convention that is typically used, namely that a *positive* bias is one where the sample is positive relative to the tip and the electrons tunnel out of the tip and into the sample. Fig. 2.2 also illustrates how the density of states affects the tunneling current given a particular d and ΔE. For a positive bias, the electrons must come from filled states in the tip and tunnel into empty states in the sample. Furthermore, the only states that can participate are the ones between the Fermi levels of the tip and sample, i.e. between E_F and $E_F + \Delta E$. Of course, when the bias is reversed the tunneling current is a probe of the filled states just below the Fermi level of the sample, i.e. between E_F and $E_F - \Delta E$. For a small bias, the density of states can be considered to be constant with respect to energy and the tunneling current varies linearly with both bias and the density of states. On homogeneous surfaces, like clean metals, the contribution to the contrast due to topography of the surface (from the exponential dependence of the current on d) is dominant and the contribution due to variations of the density of states is relatively minor. The Pt(111) surface serves as a good example; the atom to atom corrugation on a single terrace (due to changes in the density of states) is 0.1 Å while the corrugation from terrace to terrace (due to changes is height) is 2.1 Å.

The theoretical treatment of the phenomena surrounding STM is making steady progress. For example, it is possible to predict the corrugation due to various ad-atoms on otherwise clean metal surfaces. In some cases, it is also possible to calculate images for densely packed layers of adsorbates. In either case, the theory is complicated by the need to accurately describe the electronic structure of both the tip and the sample. One expects the results to depend on the structure of the sample, but it is troubling that the structure of the tip is so important. In practical terms, it means that when the experimenter does not know the exact structure of the tip (almost always the case) the level of detail about the surface that can be extracted from the images is limited. There are some cases, such as experiments done in UHV at low temperatures, where the tip structure remains constant for long periods of time. Under these conditions it is possible to pick up a molecule of known identity with the tip and use it to create the images, which solves the problem.

Not every image needs a theoretical simulation to be useful, though. As long as the lateral distances in the image are calibrated, it is possible to measure the size of a unit cell of adsorbates or count the number of defects in a semiconductor without any theoretical treatment. Such experiments will make up the majority of uses for STM until a more convenient theoretical treatment is developed.

2.2 Experimental considerations

After discussing the principle of vacuum tunneling we will turn to the practical considerations of STM. First is a discussion of contrast mechanisms where we describe how one uses the vacuum gap to create an image. This section illustrates one of the reasons that STM is so popular: a single instrument, used in slightly different ways, can

give atomic scale information about the topography, density of states or work function of a surface.

As stated in the previous section, the principle behind the STM is quite simple, but that does not mean that STM is an easy technique to use. The crux of an STM experiment is trying to bring an atomically sharp, and therefore very fragile, tip to within a few Angstroms of the sample without permitting them to touch. Binnig and Rohrer solved this problem by attaching the tip to a piezoelectric positioner and this is still the state of the art. The small size of the vacuum gap means that it is a very sensitive detector of vibrations in either the tip or sample, which makes STM practitioners experts in vibration isolation.

2.2.1 Contrast mechanisms

A digital image is just an array of numbers, where each element in the array represents a point on the surface and the number in that element represents some physical measurement made at that point. For a digital picture made with a CCD camera, the value in each element of the array indicates the intensity of the light on the corresponding point on the CCD. With the appropriate filters, one could make an image that contained only information about the light intensity at a particular wavelength. A complete set of such images would contain more information about the subject of the picture than any single image could contain. For STM the situation is much the same. We can make our image using any one of several contrast mechanisms (analogous to using one of several filters), and by taking several images using different mechanisms we can collect much more information about the surface. In his book on scanning probe microscopy,

Wiesendanger [4] discusses at least fifteen different contrast mechanisms that can be used to create an image using an STM, but the three discussed in the following section are the most common.

2.2.1.1 Topography

As mentioned in section 2.1, the tunneling current is a sensitive indicator of the tip sample distance. We take advantage of this property to make a topographic image of the surface (one where the contrast mechanism is height). The tip is quickly (1 Å/ms) moved back and forth over the surface in the x direction while at the same time moving slowly (1 Å/s) in the y direction. A feedback circuit monitors the tunneling current (usually < 1 nA) and moves the tip up or down in the z direction to keep the current constant, thus keeping the height constant. The height of the tip is measured at a frequency much higher than the rastering frequency and averaged into the proper number of bins to give the desired resolution for the image. Typically, a 100 Å by 100 Å image would be taken over the course of 100 seconds and used to produce an image with either 256 by 256 pixels or 512 by 512 pixels. Fig. 2.3a shows a schematic diagram of a topographic mode image being taken. As the tip moves over the atoms that are protruding from the surface the tip-sample distance decreases and the current begins to increase exponentially. This signals the feedback circuit to withdraw the tip in order to maintain the current constant. As the tip moves over the lower sitting atoms the opposite occurs, and the tip moves toward the surface. This process produces a single line in the image. A computer then translates the height of the tip into the brightness of the corresponding pixel on the screen. For large scale, low-resolution images, this description is sufficient to explain the meaning of topographic STM images.

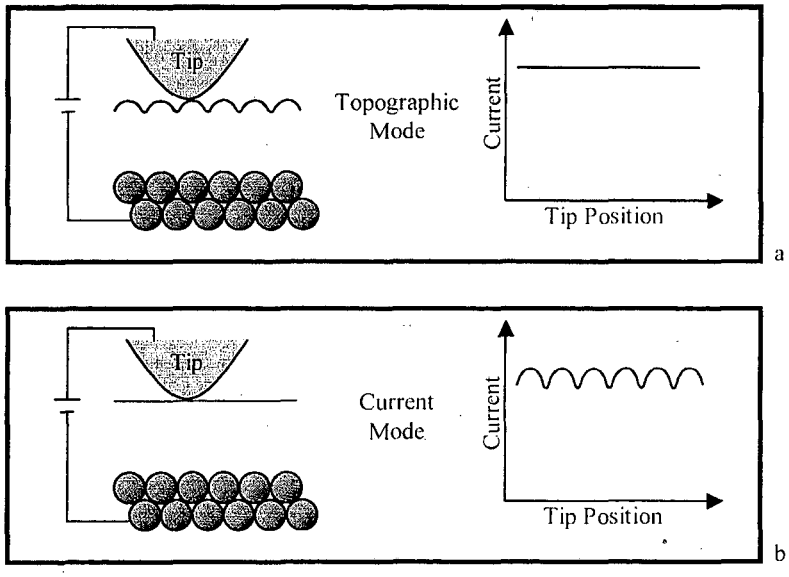

Figure 2.3 Diagrams of topographic and current mode imaging. Topographic mode images (a) are taken with a fast feedback loop which maintains the current constant. Current mode images (b) are taken at high scan speeds with a slow feedback loop, which allows the height of the tip to remain constant.

Even a cursory examination of Eq. 1 reveals that calling this mode of STM "topographic" is a misnomer. The topography of the surface is usually the most important contribution to the contrast in this mode, but there are also effects due to changes in the work function and density of states (DOS) of the surface, not to mention tip effects. One famous example is the case of oxygen adatoms on Pt(111); the oxygen atoms on the surface sit slightly higher than the surrounding platinum atoms, but they appear as dark spots (depressions) in the STM images. Two molecules with the same height can give two different apparent heights in topographic STM images; one example would be CO and NO on Rh(111) in Chapter 8. Finally, the same molecule can appear to have two different heights depending on its surroundings as is the case for NO on Rh(111). When it is sitting on a surface where the coverage is low it has a high corrugation, but when the coverage is high the corrugation drops by a factor of ten.

Since the surface in topographic mode STM images is not strictly a surface of constant tip-sample distance it is probably better to abandon the semi-classical analysis of Eq. 1 and describe the system quantum mechanically when interpreting high resolution images. According to Wiesendanger [4], the tunneling current can be described by

$$I \propto \exp(2\chi R) \cdot \sum_{v} \left|\Psi_v(\hat{r}_0)\right|^2 \delta(E_v - E_F), \qquad 2.2$$

when the bias is small. In Eq. 2.2 R is the radius of curvature of the tip, $\hat{r}_0$ is the position of the center of the tip's radius of curvature and $\Psi_v(\hat{r}_0)$ is a surface wavefunction with energy E_v. The second term inside this equation is the local density of states (LDOS) at the Fermi level, E_F, i.e. the charge density from electronic states at E_F evaluated at the center of curvature $\hat{r}_0$ of the effective tip. The STM images obtained at low bias in the

topographic mode therefore represent contour maps of constant surface LDOS at E_F evaluated at the center of curvature of the effective tip, provided that the tip is well represented by an s-type orbital.

2.2.1.2 Current

Fig. 2.3b shows a schematic diagram of current mode imaging. Current mode images are taken by increasing the scan rate and decreasing the feedback time-constant so that the feedback loop does not significantly move the tip relative to the surface during the time used to scan one image. In this mode the feedback loop only corrects for thermal drift in order to keep the tip from crashing into the surface. As the tip moves over the surface, atoms that are protruding toward the tip will cause the current to increase. Thus, an image can be produced by recording the current as a function of position.

The primary advantage of current mode imaging is that the scan rates can be several orders of magnitude higher than with topographic mode imaging. In topographic mode imaging the scan rate is limited by the speed of the feedback loop. Current mode imaging is not limited in this way, so the scan speed can be increased by about three orders of magnitude. The practical limit for the rate at which current mode images can be taken is set by the speed of the data acquisition system, but could be as high as 10 to 100 frames per second.

At high scan rates one must be concerned with mechanical resonances in the microscope and the performance characteristics of the piezoelectric tip positioner. Scanning tunneling microscopes are typically built using light, rigid parts to make the mechanical resonances at very high frequency (above 10 kHz). As the scan speed approaches a

mechanical resonance, the microscope begins to vibrate and noise is introduced into the image. The piezo itself can also limit scan speed. The response of the tip positioner is linear for small displacements at low frequency. As the frequency increases, though, the piezo response becomes increasingly non-linear. The affect of this on the images is a stretching of the image in the fast-scan direction, which is usually left to right.

Current mode imaging has one disadvantage, which makes it less useful than topographic mode imaging: it can only be done on very flat surfaces. Because the current drops quickly as the tip-sample distance increases the tip must always be within a few Angstroms of the surface. If the scan area includes a protrusion that is more than a few Angstroms tall, such as a series of atomic steps, the tip will touch the surface as is moves over the protrusion. At the very least this means that the surface has been altered because of the presence of the tip, but it could destroy the tip entirely.

2.2.1.3 Barrier height

The apparent barrier height can be interpreted, to first order, as the average value of the work functions of the tip and sample. Since the work function of the tip is constant, local changes in the apparent barrier height can be immediately attributed to changes in the electronic structure of the surface. Measuring the apparent barrier height with the STM is relatively easy, and is usually done while simultaneously taking topographic images.

Analysis of Eq. 2.1 shows that

$$\frac{\partial \ln I}{\partial d} \propto \sqrt{\Phi}. \qquad 2.2$$

In a constant current (topographic) mode image I is the same everywhere in the image, so if we simultaneously measure $\frac{\partial I}{\partial d}$ we can map changes in the barrier height using

$$\Phi \propto \left(\frac{\partial I}{\partial d}\right)^2. \qquad 2.3$$

The derivative of I with respect to d can be taken electronically by oscillating the tip in the z direction while simultaneously measuring the oscillation in I at the same frequency. This is done by driving the tip positioner with a small AC signal so that the amplitude is an Angstrom or less; the amplitude of the oscillation in I is proportional to $\frac{\partial I}{\partial d}$. As long as the driving frequency is high enough the feedback loop will not respond to it and the (topographic) image quality will not be compromised. Even though the image will not be affected the motion of the tip will cause an oscillation in the current, which can be measured using a lock-in amplifier. The lock-in signal is proportional to $\frac{\partial I}{\partial d}$, so mapping the square of the lock-in signal as function of position gives the barrier height image.

Barrier height imaging is very useful for separating the corrugation effects due to topography from those due to the electronic structure of the surface. Imagine a topographic image of a binary surface alloy. Some of the surface atoms appear brighter or higher than the rest, but we do not know if this is due to strain in the lattice near the substitutional sites or from a difference in the work function of the two metals. If the barrier height image shows no contrast, then we know that the brighter atoms are actually sitting higher than the rest of the surface.

Since the barrier height image is not taken at constant tip-surface distance we cannot perfectly decouple topographic and barrier height effects. Scanning at constant average current (and constant bias) implies that the product $\sqrt{\Phi} \cdot d$ is kept constant, rather than d. However, since the spatial variation of the barrier height is small, and it enters only under the square root, the spatial variation of the barrier height is measured at an *almost* constant tip-surface distance.

2.2.2 Piezoelectric tip positioning

Since the invention of STM in 1982 there have been several different STM designs. Our instrument is of the Beetle design, invented by Besocke and it uses piezoelectric tubes for both the course and fine tip positioning.

Piezoelectric materials change shape when an external potential is applied to them. This is not an uncommon property for a material to have, quartz is piezoelectric for example, but the tubes in an STM are made of lead zirconate lead titanate or PZT. The PZT tube is coated inside and out with zinc, which acts as an electrode; the coating on the outside is divided lengthwise into four sectors. In order to maximize the response of the piezo tube it is polarized by applying a large voltage (800 V) between the inside and outside perhaps while heating to 110 °C, or so. It is held under these conditions for 8 to 12 hours to allow the ferroelectric domains to align themselves to the applied field. When the tube is cooled and the voltage removed it maintains this polarization indefinitely as long as the temperature remains below the Curie point of the material, which is 365 °C.

The displacement of the tube due to an applied potential depends on the shape of the tube and how it was polarized. If the tube was polarized with the outer electrodes positive,

then a positive potential applied to the inside of the tube will cause the tube to expand. The change in length of the tube is $\frac{\Delta L}{L} = d_{31}\frac{V}{w}$, where w is the wall thickness, V is the voltage and d_{31} is the piezoelectric coefficient, which for PZT is 1.71 Å/V. A lateral displacement is achieved by applying a bias between two opposite sectors on the outside of the piezo, one positive and one negative relative to the inner electrode. The lateral displacement (toward the positive electrode) is then $\Delta xy = 2\sqrt{2}\cdot d_{31}\frac{L^2 V}{\pi D w}$, where D is the inner diameter of the tube.

The tip positioning is done using four identical piezo tubes attached to a freestanding head, shown in Fig. 2.4. The three outer piezos (labeled A) support the head and are tipped with glass or sapphire balls (called feet). The scan piezo (B), which holds the tip, is in the center of the scan head. The head rests on a sample holder (C), which has three helical ramps for the coarse approach and holds the sample in the center (D). The ramps have a height of 1 mm from top to bottom, so the tip moves a vertical distance of 1 mm as the head turns 1/3 of a turn. The coarse approach begins with each foot at the top of its ramp and the tip approximately ½ mm away from the surface. The head "walks" down the ramp by turning clockwise until the tip is within tunneling range of the surface. The motion is produced by slowly bending the legs in the direction tangential to the edge of the ramp, then quickly snapping them straight. When the legs snap straight the feet slide across the ramp into position for the next step. The magnitude of the bending motion and the stepping frequency can both be varied to adjust the approach rate. During the step, the tip is retracted and between steps it is advanced by the scan piezo. If no tunneling current is detected, the tip is retracted for another step. As long as the vertical motion of

each step is smaller than the z range of the scan piezo (approximately 5000 Å), there is no danger of the tip touching the surface during this process. A similar process is used to walk the head in the x or y direction.

Most of the tip positioning is done using the scan piezo when the tip is in tunneling range of the surface. The x- and y-ranges of the scan piezo are 5 μm. Since this range is used for both the offset and the image rastering, full size images can only be taken in the center of the scan range. The z-position of the tip is adjusted by the feedback loop automatically, but a voltage applied to the inner sectors of the walking legs sets the z-offset. This makes the STM head rise up (or squat down) as a unit, which allows the feedback circuit to use the full z-range of the scan piezo to prevent a tip crash.

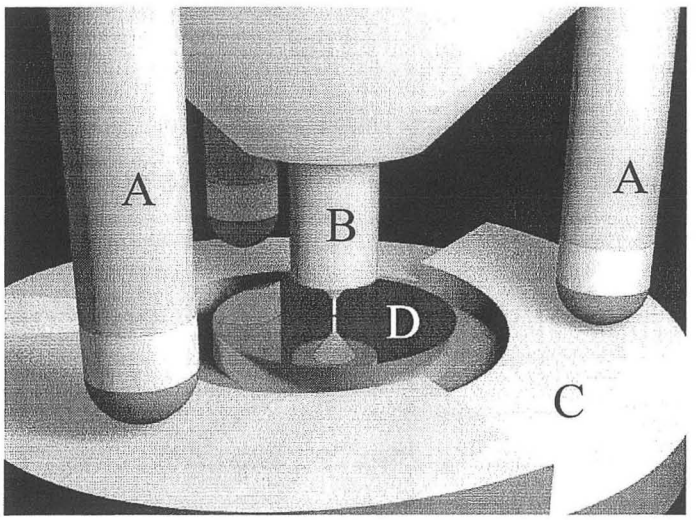

Figure 2.4 Drawing of an STM scan head. The three outer piezos (labeled A) support the head and are tipped with glass or sapphire balls (called feet). The scan piezo (B), which holds the tip, is in the center of the scan head. The head rests on a sample holder (C), which has three helical ramps for the coarse approach and holds the sample in the center (D).

2.2.3 Noise sources

The noise level in an STM determines the vertical resolution of the instrument. There are several possible sources of noise including electrical, vibrational and chemical.

The tunneling current is often less than 1 nA, so it must be amplified by six orders of magnitude before it can be transmitted without significant losses. This is done by using a current to voltage converter with a typical gain of 1 mV/nA. Because of the high gain in the amplifier, even tiny stray electrical signals picked up by the amplifier could easily mask the true tunneling current. Electrical noise can also be introduced into the tunneling current through the piezo drive signals. This causes the tip (or the whole scan head) to oscillate in response to the noise, which generates noise in the tunneling current signal. Since even seemingly minor changes in the apparatus can change the grounding configuration of the STM system, constant attention must be paid to minimizing sources of electrical noise.

As discussed in the next section, mechanical vibration can be a serious problem in scanning tunneling microscopes. Vibrational noise can be introduced into the microscope by propagating through chamber itself or a loose component on the scan head could generate its own vibrations. Sources of vibrational noise are often more difficult to isolate than sources of electrical noise. Electrical noise can be effectively measured and quantified with an oscilloscope, but the analogous device for vibrational noise, an accelerometer, is not nearly as effective.

Chemical noise is not a serious problem for experiments done at low temperature and pressure, but it is the single biggest source of noise in high-pressure conditions. Gas molecules moving between the tip and sample cause noise by changing the tunneling probability through the junction. Gas molecules arrive at the tunneling junction with a frequency that scales linearly with the pressure; in UHV there might be several minutes between the arrival of one molecule and the next, but at 500 Torr it is much more frequent. At low temperatures, many molecules cannot diffuse on the tip and sample, which also decreases chemical noise. The diffusion of adsorbates on the tip and sample is also inhibited by very high coverages, which is the situation one would expect in high-pressure experiments. This issue is discussed in more detail in Chapter 3.

2.2.4 Vibration isolation

Because the tunneling current is very sensitive to changes in the tip-surface distance, the STM is a good vibration detector. The theoretical vertical resolution of the STM is in the 0.1 pm range, but in order to achieve this the tip-surface distance must be stable to less than 0.1 pm. This is normally done with three design features of the STM system. First, the head is built small and rigid. This makes it stiff enough so that it does not respond dramatically to vibrations. Second, the STM stage, which holds the sample and the STM head, is decoupled from the chamber with Viton spacers. Viton is soft enough to dampen the high frequency vibrations in the chamber due to acoustic noise but is stiff enough to hold the STM stage still for sample transfer and tip exchange. Third, the chamber is isolated from the floor by pneumatic air legs. Normal floor vibrations have amplitudes of about 1 μm at a frequency of a few Hz, so the STM must be effectively decoupled from the floor. Air legs block about 90% of the floor vibrations.

2.3 *High pressure STM on catalytic systems*

2.3.1 Reconstruction of Pt(110)

Some of the first in-situ STM experiments were done by McIntyre, et. al. in 1993 [5]. Their apparatus consisted of an ultra high vacuum (UHV) system with a "vacuum suitcase", which allowed the sample to be transferred into a reaction cell while maintaining low vacuum (10^{-5} Torr). After cleaning a Pt(110) in vacuum and transferring it into the reactor, which was equipped with an STM, they introduced 1.6 atm of hydrogen and heated to 425 K for 5 hours. After the sample was cooled to room temperature, STM images showed that the surface had reconstructed into small facets. The terrace size of these facets indicated a ($n \times 1$) reconstruction where n is 2 to 5. The hydrogen was replaced with oxygen and heated again. After cooling, the surface had reconstructed into 100 Å to 300 Å terraces. A similar experiment in carbon monoxide yielded unreconstructed (110) terraces separated by multiple height steps. They did not achieve atomic or molecular resolution of the metal surface or the adsorbates; the factor that limited the resolution of these experiments seems to be the radius of curvature of the tip. This is not surprising considering that the only way that the sample could be heated was by heating the entire reactor from the outside. This means that the tip was exposed to the same pressure and temperature conditions as the sample. Even if their Pt/Rh wire was initially sharp, it would reconstruct, just as the surface did, giving a large radius of curvature.

Despite the limitations of this instrument, it continued to produce interesting results. These include the first demonstration of tip catalysis and a study of the morphology of coke on the surface of a model catalyst.

2.3.2 Tip catalysis – hydrogenation

Platinum is a common tip material in STM experiments. It does not form a surface oxide in air, so it can be prepared by just cutting a platinum wire at a shallow angle. Since Pt is also catalytically active, it can be used to control a chemical reaction on the nanometer scale. This was first demonstrated by McIntyre, et. al. by reacting carbon clusters with gas phase hydrogen using an STM tip [6].

Propylene adsorbs on the Pt(111) surface forming propylidyne ($\equiv C\text{-}CH_2\text{-}CH_3$). When the surface is heated, much of the propylidyne dehydrogenates to form carbonaceous clusters. McIntyre imaged a surface covered with these clusters in 1 atm of hydrogen and observed that the clusters appear as 3 Å tall bright spots in the images. Under these conditions, the Pt/Rh tip is coated with a layer of carbon and is not catalytically active. When a voltage pulse (0.9 V) was applied to the tip, the tip became active and removed the carbon clusters from the surface. The carbon clusters were removed only on the areas of the surface that were being imaged with the "cleaned" or "activated" tip. After a few minutes the tip was contaminated again and was deactivated. Large scale images taken after tip deactivation showed that the scan area that was being imaged with the active tip was free of carbon clusters while the surrounding surface was unchanged. This experiment showed that STM could be used as a chemical nanopatterning tool, not just as an imaging technique.

2.3.3 Tip catalysis – oxidation

Catalytically active STM tips can also oxidize carbon on the surface. In an experiment that parallels the one above, carbon deposits on a Pt(111) surface were oxidized by imaging them with a Pt/Rh tip in a high pressure oxygen environment [7].

The mechanism by which the tip oxidizes the carbon on the surface is not known. The authors of Ref. 7 suggest that the tip acts as a source of oxygen atoms because the active tip dissociatively adsorbs oxygen, then delivers it to the surface. Because inert tips like gold or deactivated platinum do not react away the carbon, we know that the mechanism is chemical in nature. It is possible, though, that other systems might undergo chemical changes because of the high electric field under the tip or from the electrons tunneling into otherwise unoccupied orbitals of the adsorbate layer.

2.3.4 Hydrogen induced restructuring of Cu(110)

The first atomic resolution images of a catalytically active metal surface in a high-pressure environment were taken by L. Osterlund, et. al. [8]. They showed that the Cu(110) surface maintains its (1×1) structure in hydrogen up to 20 mbar, then undergoes a phase transition to a (1×2) structure. The (1×2) phase remains even if the pressure is increased to 1 bar but disappears when the pressure is decreased. Since the Cu(110)-(1×2)-H structure is well known from UHV studies at low temperature and pressure, the authors concluded that it is possible, in general, to predict the high pressure, high temperature structures by extrapolating from experiments done in low pressure, low temperature environments.

In high-pressure environments, the surface coverage of adsorbates is high because the gas and surface are in equilibrium. Surface science is most often done in low-pressure environments because they depend on beams of electrons or particles. In order to achieve high surface coverages in low-pressure environments, the temperature of the surface must be decreased to prevent the molecules from desorbing. All of this is done under the common assumption that raising the pressure is equivalent to lowering the temperature. Experiments like the one described here serve to reinforce this idea.

---

1 G. Binnig, H. Rohrer, Surf. Sci. **126,** 236 (1983)

2 G. Binnig, H. Rohrer, C. Gerber, E. Weibel, Phys. Rev. Lett. **50,** 120 (1983)

3 K. Christmann, Introduction to Surface Physical Chemistry, Springer-Verlag, New York (1991)

4 R. Wiesendanger, Scanning Probe Microscopy and Spectroscopy, Cambridge Univ. Press (1994)

5 B. J. McIntyre, M. Salmeron, G. A. Somorjai, J. Vac. Sci. Tech. **11,** 1964 (1993)

6 B. J. McIntyre, M. Salmeron, G. A. Somorjai, Science **265**, 1415 (1994)

7 U. Schroder, B. J. McIntyre, M. Salmeron, G. A. Somorjai, Surf. Sci. **331,** 337 (1995)

8 L. Osterlund, P. B. Rasmussen, P. Torstrup, E. Laegsgarrd, I . Stensgaard, F. Besenbacher, Phys. Rev. Lett. **86,** 460 (2001)

3 Experimental Apparatus

The design and performance of a high pressure, high temperature scanning tunneling microscope (HPHT-STM) system is described here. The system combines a UHV surface analysis/preparation chamber with a variable pressure (5×10^{-10} Torr to 1 atm) and temperature (300 K to 675 K) STM. The STM chamber can be isolated by three gate valves and filled with one atmosphere of any gas mixture. A load-lock mechanism allows the transfer of samples and tips into the chamber without exposing them to air. Heating at high pressure is achieved using a halogen lamp beneath the sample. The performance of the instrument in high pressure and temperature conditions is demonstrated by imaging a Pt(111) single crystal in nitrogen.

3.1 Introduction

The structural properties of catalytic metal surfaces have traditionally been investigated by surface science techniques in UHV before and after the metal surface has been used to catalyze a reaction. The high-pressure gas environment of reaction conditions is incompatible with most surface analysis techniques, so the *in situ* examination of the surface is difficult. Techniques such as scanning tunneling microscopy (STM) [1,2,3], sum frequency generation (SFG) [4,5,6,7] and UV raman spectroscopy [8,9,10], which are not limited to vacuum, have been employed in high pressure and temperature investigations. For example, previous STM studies of metal single-crystal surfaces exposed to high pressure (~ 1 atm) and high temperature (~ 425 K) have shown dramatic changes of surface structure that are not observed below 10^{-4} Torr [3]. Recent *in situ*

surface vibrational studies of the CO + O_2/Pt(111) system using SFG [4] have identified surface species present only during catalytic conditions (high reactant pressure and high temperature), implicating them as intermediates to CO_2 production. These high-pressure results could not have been predicted from extrapolation of results obtained in low-pressure (less than 10^{-4} Torr) conditions.

We have developed an apparatus that combines a high pressure, high temperature scanning tunneling microscope (HPHT-STM) with a UHV surface analysis chamber. This combined UHV and high-pressure chamber, together with an improved heating system, represents a major improvement over our previous HP-STM apparatus as it allows sample transfer without contamination by exposure to air. This chapter discusses design considerations and the performance of the HPHT-STM. To illustrate the capabilities of this instrument, results are shown from investigations of the Pt(111) and Rh(111) surfaces under high pressure and temperature conditions.

3.2 Apparatus

The system is divided into three parts: (1) a UHV surface preparation and analysis chamber, (2) a variable pressure STM chamber and (3) a load lock and sample transfer system. A schematic of the entire system is shown in Fig. 3.1. A 260 L/s molecular turbo pump (Balzers-Pfeiffer, Model TMU 260) is attached below the STM chamber and can be used to pump any one or all of the three sections. The entire system is supported by a wooden frame that rests on four pneumatic air legs (Newport Laminar Flow Isolators, I-2000 Series) for primary vibration isolation.

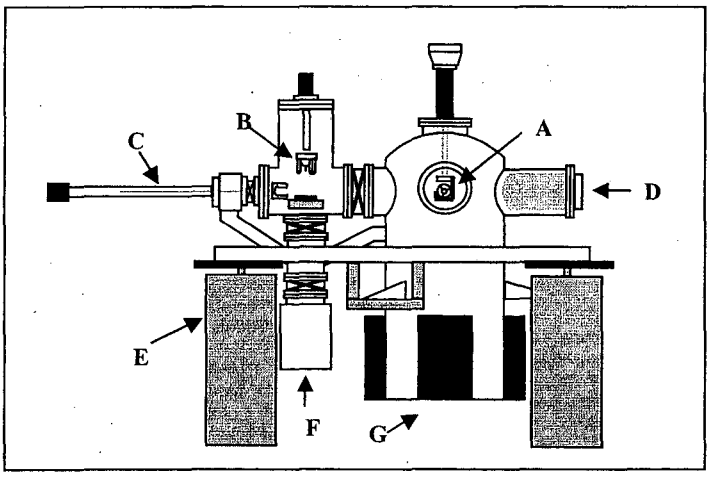

Figure 3.1 HPHT-STM System schematic. **A** UHV sample manipulator with electron beam heating and cooling, **B** Variable temperature STM, **C** Magnetically coupled linear-rotary transfer arm, **D** CMA for AES (QMS, LEED optics, and Ar ion gun not shown), **E** Pneumatic air legs and suspension frame, **F** 260 l/s turbo molecular pump, **G** 150 l/s ion pump. The "X"s represent UHV gate valves.

3.2.1 UHV Chamber

The UHV portion of the apparatus is a standard Varian surface analysis chamber equipped for Auger electron spectroscopy and quadrupole mass spectrometry, as well as Ar^+ ion sputtering and electron beam heating for sample cleaning. The UHV chamber is pumped by a 200 L/s ion pump and a liquid N_2 cooled titanium sublimation pump which provide a working base pressure of 5×10^{-10} Torr.

3.2.1.1 Auger

Auger electron spectroscopy (AES) is a surface sensitive technique, which is commonly used to determine surface composition. When a solid is irradiated with a beam of high-energy (1-10 kV) electrons, the atoms are ionized, producing an unfilled core state. An outer shell electron fills the core hole and the energy is released as a high-energy electron or a photon when the atom relaxes. The process that results in the production of an electron is called the Auger process, and the energy of the Auger electron is a characteristic of the atom. An energy selective electron detector is used to determine the Auger electron yield as a function of energy; the peaks in this plot can be used to quantitatively determine the atomic composition of the solid. The mean free path of electrons inside solids is very short (about 10 Å), so Auger electrons produced deeper in the sample are not going to escape to the surface. This is what gives AES its surface specificity.

In our experiments AES is only used to check the cleanliness of the surface before the STM experiments. The most common contaminant on our samples is carbon; the detection limit for carbon is approximately four atomic percent using our apparatus.

3.2.1.2 Mass Spectrometer

The UHV chamber is equipped with a UTI mass spectrometer. It is used primarily for residual gas analysis, but can also be used to check the purity of reagent gases.

A 4-foot long hose leads from the STM chamber to a leak valve under the mass spectrometer. Inside the vacuum chamber a 1/8" stainless steel tube leads from the leak valve to a hole in a tantalum shroud covering the mass spectrometer ionizer. This allows a controlled leak of gas from the high pressure STM chamber to be released into the shroud. The shroud makes the mass spectrometer approximately ten times more sensitive to gas escaping from the leak valve than to gas in the background of the chamber. This is very helpful to prevent interference from gas that backstreams from the ion pumps when they have a large pumping load.

We can monitor the molecular species in the STM chamber to check for gas purity or reaction products by opening a leak into the shroud and manually recording the peak heights of the relevant masses. Alternatively, we can use an 8088-based computer with a data acquisition card and simple Asyst program to automatically record the peak heights for several masses at a specified time interval [11]. The program writes the data into a text file, which can be read by Excel or another graphing package.

3.2.1.3 Manipulator and transfer system

A 36" long, magnetically coupled, linear, rotary feedthrough is used to transfer the sample between the two chambers and a load lock. The load lock and transfer system are also used to introduce new probe tips into the STM chamber.

The transfer system is designed around a sample car that holds both the sample and the approach ramps required for the walking STM. The sample car design, shown in Fig. 3.2, is based on the RHK sample car. The sample is held in the sample car by leaf springs, which are not susceptible to loosening due to thermal expansion. A type K thermocouple in a ceramic tube leads through the molybdenum ramps and is held in place by a set screw. The bare thermocouple wires protrude from the sample car approximately 4 mm and are positioned to allow them to contact thermocouple leads on the STM stage or the UHV manipulator. The interior of the sample car is lined with alumina to protect it from the intense heat of the light bulb, but a hole in the back of the ceramic spacer allows light to hit the back of the sample directly.

The UHV manipulator is an original design based on a commercial XYZ translation stage. It holds the sample holder in a vertical position on a stainless steel fork, which aligns the thermocouple leads with matching chromel and alumel contacts. Behind the sample holder, an electron beam heater filament is held in a movable carriage. The carriage is moved toward the sample holder with a rack-and-pinion gear when the sample is transferred into the UHV chamber. This places the filament less than 1 mm behind the sample, so that the electron beam heats only the crystal and not the surrounding sample holder. The front of the carriage, the portion that touches the sample holder, is a 5 mm thick piece of copper with a copper braid attached to it. The other end of the copper braid

is attached to a liquid nitrogen cooled cryostat. The cooling power of this apparatus is sufficient to hold the sample at 225 K after the liquid nitrogen has been flowing continuously for a few hours. The primary purpose of the liquid nitrogen cooling system is to prevent the sample holder from heating up when the sample is annealed for several minutes. Fig. 3.3 is a diagram of the UHV manipulator.

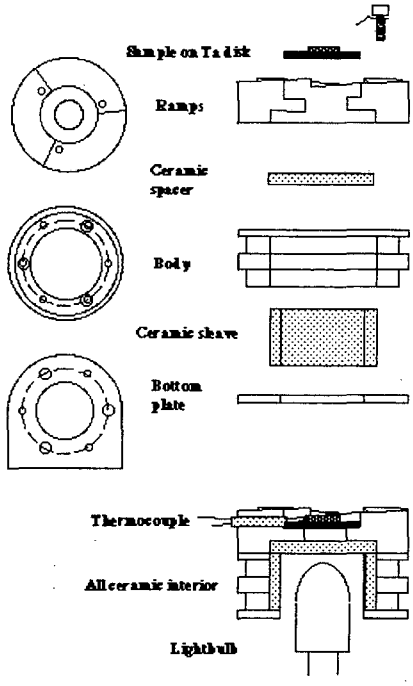

Figure 3.2 Sample mounting scheme. The sample is held to a 0.010" thick Ta plate by spot welding thin Ta straps over its edges. This assembly is held on the Mo walking ramps by three springs and the ramps are bolted to the body of the sample holder. Note that the inner surface of the sample holder is lined with alumina to minimize the damage sample holder due to the extreme heat of the lightbulb.

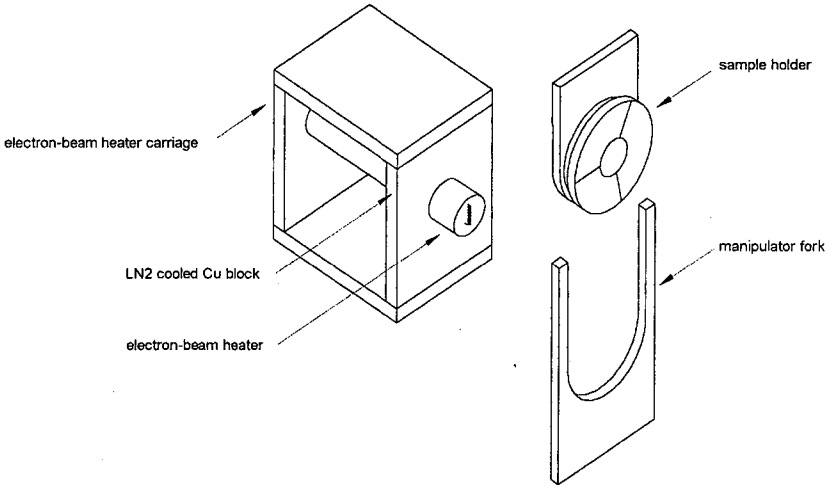

Figure 3.3 Diagram of the UHV manipulator. The manipulator fork positions the sample holder in front of the electron-beam heater carriage. A rack-and-pinion gear (not shown) moves the carriage forward so that the electron-beam filament is positioned 1 mm behind the sample. The front of the electron-beam heater carriage is a ¼" thick piece of copper, which is cooled with liquid nitrogen.

3.2.2 STM Chamber

The STM portion of the apparatus is a custom build chamber designed around the STM stage, mounted horizontally on an 8" flange, and the STM manipulator, mounted vertically on a 6" flange. Since this chamber is filled with gas during a high-pressure experiment, every effort was made to minimize its volume to about 10 L. A 2' long loop of 1/4" stainless steel tubing is attached between the top and bottom of the STM chamber. The tubing contains a rubber septum that allows us to withdraw a sample of gas from the chamber for GC analysis. Our experiments show that diffusion alone mixes the gas within the chamber and septum tube in about 10 minutes. This serves as an alternative to the gas analysis with the mass spectrometer described above.

3.2.2.1 Scan head, manipulator and STM stage

The microscope itself is a commercially available Beetle-style STM equipped with sample heating and cooling and *in situ* probe tip exchange (RHK Model VT-UHV300). The microscope stage provides secondary vibration isolation, which is essential for stability in such a large vacuum system. The STM chamber can be isolated from the rest of the system by gate valves, allowing the introduction of high gas pressures while the UHV chamber and the load lock remain in vacuum. The STM tip can remain in tunneling range as the pressure in the chamber is increased so the same area of the surface can be imaged before and after the introduction of gas. After introducing a reactive mixture of gases, the chamber is pressurized to one atmosphere with helium. A short loop of tubing containing a septum is then attached to the chamber. A sample of

gas can be withdrawn through the septum with a syringe to be analyzed by gas chromatography.

3.2.2.2 Sample heating

In order to heat the sample in high pressures (greater than 1×10^{-4} Torr), the electron beam heating filament which is standard on the RHK VT-UHV300 microscope stage was replaced by a small 360 W, tungsten filament, halogen filled, quartz bulb. This provides radiative heating without making mechanical contact with the sample, preserving the vibrational isolation of the STM stage. The bulb is raised into the sample car so the top of the bulb is approximately 1 mm below the bottom of the sample. Power is provided with an alternating current transformer. This heating system can achieve temperatures of greater than 900 K in all pressures up to 750 Torr.

3.2.2.3 Tips

The chemical and thermal stability of the scanning probe tip is of primary importance under the high-pressure and high-temperature conditions of our studies. Choosing an acceptable tip material is the most challenging aspect of high-pressure STM that must be resolved for the easy application of STM to chemical reaction studies.

Tungsten tips are the best choice for most high-pressure environments. They provide stable imaging in CO, NO, hydrogen and hydrocarbons, but are not stable in oxygen or mixtures of CO and oxygen. When exposed to oxygen the surface of tungsten forms an insulating oxide, which prevents stable imaging.

Probe tips of platinum and platinum alloys (Pt/Rh, Pt/Ir, Pt/Au) are stable in high-pressure oxygen and hydrogen but are unstable in CO. As described in Chapter 9, the metal atoms on the surfaces of platinum and rhodium are often mobile when they are exposed to high pressure CO. Presumably they form metal carbonyls, which are mobile on the surface. The result is that the STM tip is continuously changing during the experiment, often several times per minute. Eventually, a stable configuration is reached, but this usually results in a tip with a very large radius of curvature, which reduces the resolution of the images. The low resolution of the images in [1] is probably caused by this effect.

Electrochemically sharpened gold tips provide the chemical stability required for STM studies in high pressure mixtures, but they are more susceptible to blunting than tungsten tips, especially at high temperature. We prepare gold probe tips by etching 0.010" diameter gold wire in ~3 M HCl using a 1.5 V DC bias and tungsten tips in ~25% KOH solution using a 1.3 V DC bias. The etching process takes about 30 minutes under these conditions. The tip is then rinsed in water and methanol then immediately placed in the vacuum chamber.

Several other tip materials were tried, but none of them worked reliably. These included carbon coated tungsten, Rh, Ta, Au/Cu and Pd/Ru. Unlike bulk materials, STM tips cannot be improved by using alloys of different metals. For example, gold is soft, but Au/Cu alloys are much harder, so it seems as if this would make a good tip material. When we used them, though, the tips either behaved were too soft, like pure gold, or they became insulating in oxygen, like copper. The fundamental problem is that the working part of the STM tip is only the first 3-4 atoms, which are either gold or copper, so the tip

takes on the properties of one or the other of the alloy constituents without inheriting the beneficial bulk properties of the alloy. Instead of being an improvement over pure materials, alloy STM tips seem to take on the worst properties of both components.

3.2.2.4 Instrument capabilities

The system was used to examine a highly stepped (cut 5° from the [111] axis) Pt(111) crystal at high temperatures and at high pressures of N_2, an inert gas. The sample, a Pt(111) single crystal, is cleaned in UHV by successive cycles of Ar^+ sputtering, heating in oxygen (1100-1150 K in 1×10^{-7} Torr O_2), and annealing to 1250 K in vacuum. This produces a well ordered (111) LEED pattern and AES shows less than 2% residual carbon on the surface. This cleaning method produced an array of monatomic steps with an average terrace width distribution of 40 to 100 Å. Periodic step bunching often produces one or two very wide (greater than 200 Å) terraces. Imaging a sulfur (2×2) layer gave atomic resolution images, revealing that the step edges run roughly parallel to the $[11\bar{2}]$ direction (within 5-10°).

Fig. 3.4a shows an STM image obtained with a tungsten tip in 1.2 Torr N_2 at 300 K. Comparison to vacuum images show the presence of the gas has no effect on the general step morphology.

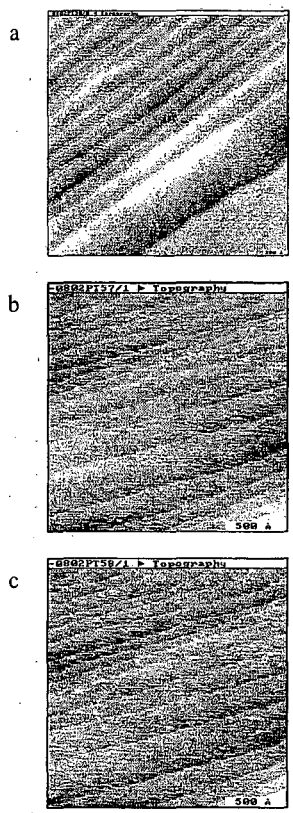

Figure 3.4 Imaging in an inert gas environment. The microscope can be used in a high pressure inert gas environment at room temperature and at elevated temperatures. Image (a) is an STM image of a highly stepped Pt(111) surface in 1.2 Torr N_2 at 300 K. Images (b) and (c) are consecutive scans of the same surface in 1.2 Torr N_2 at 574 K, showing a lateral drift of less than 100 Å/s.

The high-pressure gas does, however, affect the performance of the microscope. In vacuum the vertical resolution of the microscope is determined primarily to the vibrational noise, and thermal drift usually takes 30 – 60 minutes to dissipate. In a few Torr of gas, the mean free path of the molecules is approximately 100 nm, which means that gas molecules will frequently pass through the tunneling junction. A single molecule in the tunneling junction can have a dramatic effect on the tunneling current, increasing or decreasing it by an order of magnitude. The feedback circuit responds strongly to these sudden changes in the current by withdrawing or advancing the tip, which appears as noise in the STM image. Under high-pressure conditions this chemical noise is much greater than the vibration noise, which limits the microscope resolution in vacuum. High-pressure gas is a good thermal conductor (at least compared to vacuum), so thermal drift is less of a problem when the microscope is used at room temperature in a few Torr of inert gas. Thermal drifts are caused by thermal expansion in the microscope head and the sample holder as they come to thermal equilibrium with the chamber. In vacuum this process can take an hour, but the thermal conductivity of the high-pressure gas can shorten this time to 20 minutes.

High-pressure reactive gases (such as CO) cause the same changes in microscope performance mentioned above, but also affect the STM tips. As discussed in Chapter 9, the mobility of metal atoms in high-pressure reactive gas environments is much greater than in vacuum. Since only the last few atoms on the end of the tip affect the tunneling current, it is very sensitive to the tip's structure. When one of the metal atoms on the tip moves, it causes a change in the tunneling current, which introduces another type of

chemical noise into the image. In addition, as the metal atoms are removed from the end of the tip, it becomes blunter, which lowers the horizontal resolution of the microscope. As discussed in the previous section, the particular metal that is used for an STM tip can affect the degree to which reactive gas environments will affect the microscope's performance. Etched tungsten tips can be used in CO or CO + NO mixtures, but their useful lifetime in these environments is much shorter than in vacuum. Many tungsten tips fail immediately when they are exposed to CO, but those that do not fail can be used for 2 or 3 experiments before they become blunt. Between high-pressure experiments, the tip is cleaned in vacuum by field emission, which also indicates the aspect ratio or sharpness of the tip. A freshly etched tip that has been exposed to air for just a few minutes before being placed in the vacuum chamber might generate 1 nA of field emission current at 600 V, while a well used and blunt tip might require 1500 V to obtain the same current. Every exposure to high pressure CO increases the required field emission voltage by a few hundred volts; after approximately four exposures the tips become blunt, and more than 2500 V is needed to generate 1 nA of current. Our apparatus has no mechanism for resharpening tips inside the vacuum chamber, so blunt tips must be replaced.

The microscope's performance in vacuum at high temperature was briefly tested and found to be acceptable. The chemical noise due to faster motion of the molecules on the surface was only slightly greater, perhaps because the greater thermal energy of the molecules was offset by the lower coverage. The most substantial difference between room temperature and elevated temperature imaging is the greater thermal drift at high temperature. As the sample holder is heated, it expands so that the sample appears to be

drifting away from the tip. The thermal expansion greater than the z-range of the scan piezo when the sample is heated just 10 K, so is safest if the tip is retracted before power is applied to the heater. After 30 minutes of constant heating, the thermal drift slows enough so that the feedback can correct for the drift and keep the tip in tunneling range without crashing it into the surface. It takes more than 60 minutes for the drift to slow to the point where images can be taken. Of course, the thermal drift is in the opposite direction when the sample is cooled, so the tip must be retracted before the power to the heater is decreased. Failure to retract the tip before cooling the sample always results in a crash unless the cooling rate is just a few degrees per minute and the head is manually retracted to correct for the thermal drift. In principle, a patient STM operator could heat and cool the sample while imaging the same area of the surface by using a very low heating rate and continuously adjusting the tip height.

As mentioned above, thermal drift problems are decreased by the presence of thermally conducting, high-pressure gas. Fig. 3.4b and 3.4c show the same surface as Fig. 3.4a after it was heated to a stable temperature of 574 K in the N_2 gas and re-imaged. Consecutive scans taken 20 minutes later show the lateral drift to be less than 100 Å/minute at this temperature and pressure. The general step morphology is unchanged by these conditions, also.

Thermal drift is a smaller problem at high-pressures, but the chemical noise is much greater. The rapid motion of adsorbate molecules at high temperature is partly compensated by lower coverage when the sample is heated in vacuum, but at high-pressure the coverage remains near saturation and there is no such compensation. The result is that the chemical noise leaves little chance of achieving molecular resolution in

HTHPSTM experiments on systems with STM corrugations less than approximately 0.1 Å. This is a fundamental limitation of the technique, but there are systems which exhibit larger corrugations and can therefore be studied with HPHTSTM, see Chapter 7 for an example.

There are several pathways that gas molecules can take to get into the tunneling junction at high-pressure, causing chemical noise. They can arrive at the tunneling junction directly from the gas phase, and would be expected to do so at high rates under the conditions used for our experiments. A calculation based on the kinetic theory of gas shows that there are approximately 10^6 gas molecules colliding with each surface atom per second at 500 Torr. The bulk of the STM tip will shield the tunneling junction from some of these collisions, but one would still expect that several thousand molecules would pass through the tunneling junction during the time it takes to acquire an image. Molecules adsorbed on the surface of the sample can diffuse into the tunneling junction. The diffusion barrier for a molecule adsorbed on a surface is typically one tenth of its heat of adsorption, so molecules that have heats of adsorption less than 0.3 eV are expected to diffuse very rapidly. This fast diffusion is a serious problem if the adsorbates are the subject of interest in the STM experiment. If the subject of interest is the substrate, then it should be possible to decrease the tip-sample gap (by increasing the setpoint current and decreasing the bias voltage) so that the tip pushes the adsorbate molecules away from the tunneling junction and allows atomic resolution of the substrate without interference from the adsorbates. Fig. 3.5 is a schematic of the STM tip showing the various pathways that molecules can take into the tunneling junction.

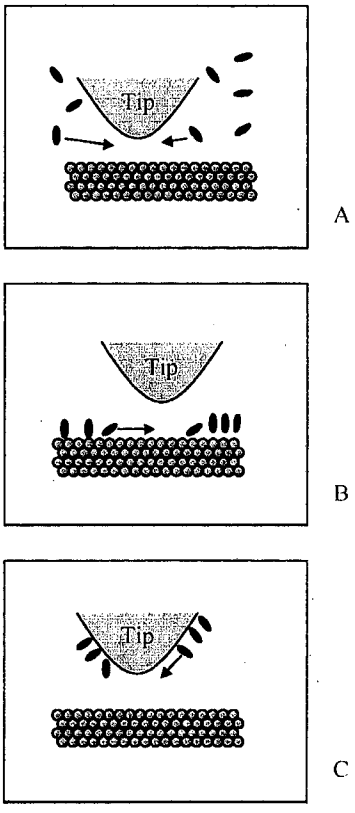

Figure 3.5 Sources of chemical noise. A) Molecules entering the tunneling junction from the gas phase B) Molecules diffusing on the surface C) Molecules diffusing on the tip

1 B.J. McIntyre, M. Salmeron and G.A. Somorjai, Rev. Sci. Instrum. 64, 687 (1993).

2 B. Marchon, P. Bernhardt, M.E. Bussell, G.A. Somorjai, M. Salmeron and W. Siekhaus, Phys. Rev. Lett. 60, 1166 (1988).

3 B.J. McIntyre, M. Salmeron, and G.A Somorjai, J. Vac. Sci. Technol. A, 11, 1964 (1993).

4 X. Su, P. S. Cremer, Y. R. Shen, and G. A. Somorjai, J. Am. Chem. Soc. 119, 3994 (1997).

5 X. C. Su, P. S. Cremer, Y. R. Shen, and G. A. Somorjai, Phys. Rev. Lett. 77, 3858 (1996).

6 P. S Cremer, X. Su, Y. R. Shen, and G. A. Somorjai, J. Am. Chem. Soc. 118, 2942 (1996).

7 P. S Cremer, X. Su, Y. R. Shen, and G. A. Somorjai, J. Phys. Chem., 100, 16302 (1996).

8 P. C. Stair and C. Li, J. Vac. Sci. Technol. A 15, 1679 (1997).

9 C. Li and P.C. Stair, Catal. Today 33, 353 (1997).

10 C. Li and P.C. Stair, Catal. Lett. 36, 119 (1996).

11 Asyst is a data acquisition package written by Sofware Technologies Inc that has a simple, assembly-like programming language.

4 Pt(111) in CO

This chapter describes how scanning tunneling microscopy was used for studies of adsorbates on model catalysts at elevated pressures. One of the most unique aspects of these experiments is that the adsorbate structures were determined under conditions where the gas and surface are in equilibrium, unlike UHV experiments where the coverage is maintained by cooling the surface. A new structure due an incommensurate hexagonal overlayer was observed for CO on the Pt(111) surface in the 200-750 Torr pressure range. When the pressure is decreased below 200 Torr, the incommensurate structure disappears, which is a behavior expected of adsorbate layers in equilibrium with the gas phase. This structure has not been observed before at similar coverage under low-pressure and low-temperature conditions. These results illustrate the non-equivalence between the structures formed at low temperature and low pressure and the equilibrium structures formed at high pressure and room temperature.

4.1 Introduction

The development of new atomic resolution imaging and spectroscopic techniques that can operate in environments other than vacuum is opening the important area of surface science at high pressures. Scanning tunneling microscopy (STM) is capable of atomic scale resolution in atmospheric pressure regimes, providing a much sought-after link between decades of ultra high vacuum (UHV) studies and the results of catalysis research performed in the realistic conditions of high reactant pressure [1]. The link over the pressure gap of many orders of magnitude that separates these two complementary fields

is extremely important because many of the UHV results cannot be extrapolated to high pressure and *vice versa*. Examples of advances in high pressure imaging are the studies of the atomic structure of passivating sulfur monolayers on Mo(001) in air [2], the high pressure driven reconstructions of Pt(110) in atmospheric pressures of O_2, H_2, and CO [3] and the opening of the new field of tip-catalyzed reactions in O_2 and H_2-hydrocarbon mixtures [4,5].

None of these previous high-pressure STM studies have determined the structure of molecular adsorbates in equilibrium with the gas phase. It has often been argued that experiments operating at cryogenic temperatures in high vacuum conditions simulate the high surface coverage of adsorbates that is prevalent at high pressures. However, the structures formed under these conditions are, by necessity, not in equilibrium with the gas phase. They might correspond to kinetically trapped structures with no similarity to structures that are thermodynamically stable at high pressure and temperature. An example of this is the adsorption of CO on metal surfaces, which has been the object of numerous studies in the past [6,7]. The known structures of CO on Pt(111) are summarized in Table 4.1.

Here we present the results obtained for this molecular adsorbate on Pt(111) in the pressure range of 200-750 Torr. Our data illustrate very clearly the fundamental differences that can be expected between the low temperature/low pressure and ambient temperature/high pressure regimes even if they correspond to a similar surface coverage.

Surface Structure	Coverage	Adsorption Sites	Reference
(2×2)	0.25	Top	8
$(\sqrt{3}\times\sqrt{3})$R30°	0.33	Top	7
c(4×2)	0.50	Top, Bridge	7, 9
$(\sqrt{7}\times\sqrt{7})$R19.1° electrochemical	0.57		17
$(\sqrt{2/3}\times\sqrt{2/3})$R15°	0.58	Top, Bridge	7
Incommensurate	0.592		10
$(\sqrt{19}\times\sqrt{19})$R23.4° electrochemical	0.685	Asymmetric near-Bridge	16

Table 4.1 The known adsorption structures of CO on Pt(111).

4.2 Experimental procedure

We used platinum single crystal sample, which was cut 5° from the (111) orientation. This highly stepped sample was chosen in order to increase the likelihood of observing changes in step morphology and refaceting caused by high pressure adsorbates, however, such effects were not observed. It was cleaned by successive cycles of Ar^+ sputtering, heating in oxygen (700-750 °C in 1×10^{-7} Torr O_2), and annealing to 950 °C in vacuum. The STM tips were electrochemically-etched tungsten treated in vacuum by field emission. A typical experiment was performed as follows: after preparation, the sample was transferred to the STM chamber and imaged first under vacuum. The images reveal the expected surface topography consisting of arrays of (111) terraces separated by single atomic steps with an average terrace width distribution of 40-100 Å. The STM chamber was then isolated from the rest of the system and CO was introduced at a rate of ~1 Torr/sec. The surface was allowed to equilibrate in the high pressure of CO for 1 hour prior to imaging. This greatly improved tip stability for imaging, presumably due to the formation of a stable passivating thin oxide or carbide.

4.3 Images and image analysis

Images of the surface acquired in up to 750 Torr of CO reveal a step morphology that is similar to that seen in vacuum in the absence of CO (not shown). Enlarged views of the terraces showed no ordered structures due to CO until the pressure reached 200 Torr. At this pressure and above, a nearly hexagonal periodic structure was formed, as shown in

Fig. 4.1, obtained in 200 Torr of CO. This structure is observed only in the presence of CO, and has a periodicity that varies from 11 ± 1 Å in some areas of the surface to 14 ± 1 Å in other areas, with a corrugation of 0.30 ± 0.05 Å. Imaging was performed at 0.1-0.2 V sample bias and 0.5-1.0 nA tunneling current with a gap resistance of 200-240 MΩ. Changing either bias or current so that the gap is less than 200 MΩ caused the hexagonal pattern to disappear. It was recovered, however, upon restoring the initial high gap condition. Presumably the tip gets too close to the surface at this low gap resistance and displaces the CO. Evacuation of the CO gas to 1×10^{-4} Torr base pressure completely removed the hexagonal pattern. An important observation is that the angular orientation of the hexagonal pattern is maintained rigidly from one terrace to the next, as seen in Fig. 4.1. Separate STM experiments on the same surface covered with a sulfur (2×2) layer [11] indicate that the average step direction is roughly parallel to the $[11\bar{2}]$ direction (within 5-10°). This indicates that the hexagonal structure close-packed rows are aligned with the Pt(111) compact [110] directions.

This high pressure structure was also examined on a less stepped Pt(111) crystal which provided terrace widths on the order of 1000 Å. This crystal was exposed to a mixture of 150 Torr CO and 50 Torr O_2, heated to 183 °C for 10 minutes, and then cooled slowly (~ 1 hour) and re-imaged. This temperature is not sufficient to ignite the CO oxidation reaction on platinum [12], but it is sufficient to desorb CO from the surface. STM images again revealed a hexagonal structure, however the annealed structure was better ordered with a more uniform spacing of 12 ± 1 Å, as shown in Fig. 4.2. As on the highly stepped sample, the hexagonal structure showed only one rotational orientation. The insert in Fig. 4.2 shows a triangular one-atom deep hole and a neighboring triangular island of

platinum, the step edges of which form 60° angles, as expected for [110] compact step edges. Examination of these step alignments show that the hexagonal structure close-packed rows are aligned (± 5°) with the [110] direction of the Pt(111) lattice.

Several attempts were made to image the surface at elevated temperatures (50 °C) and none were successful. There are several possibilities that could explain this. The most mundane possibility is that the heater (lightbulb under the sample) could have caused enough electrical noise to obscure the 0.1 Å amplitude of the ordered structure. It is also possible that the higher temperature increased the speed of the molecules enough so that the chemical noise in the microscope obscured the structure. The equilibrium structure of CO on Pt(111) at 50 °C could be disordered, or could include a large number of vacancies, which allow fast diffusion of the remaining molecules. In either case the STM could not be expected to resolve the adsorbate structure.

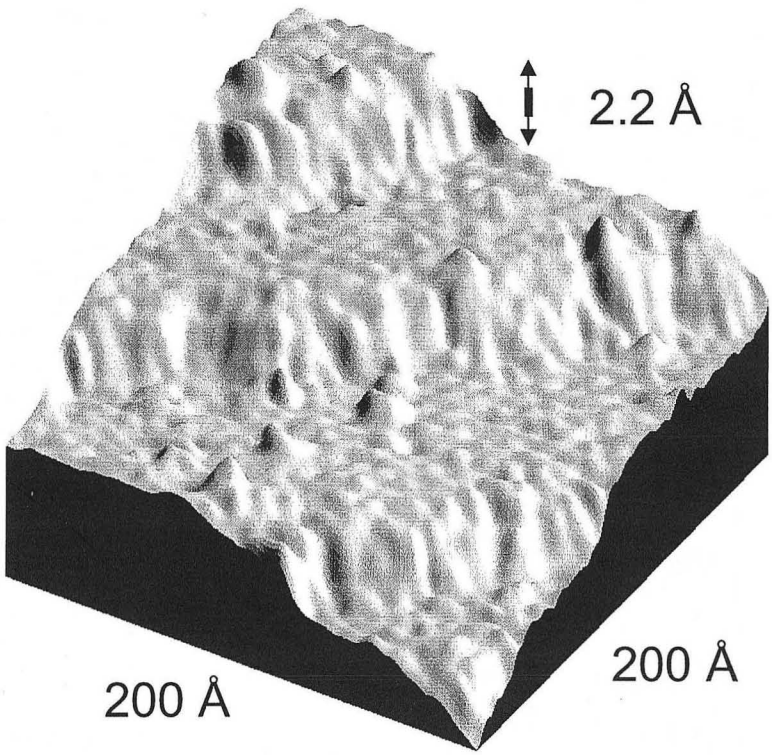

Figure 4.1 3D representation of an STM image obtained in 200 Torr CO. Image size is 200 Å x 200 Å, sample bias, V_S, is +109 mV, and tunneling current, I_T, is 0.52 nA. Height scale is greatly exaggerated to display corrugation on the terraces. Hexagonal arrays of maxima can be observed on each terrace due to a CO monolayer forming a Moiré structure. The alignment of the hexagonal array is the same in each terrace.

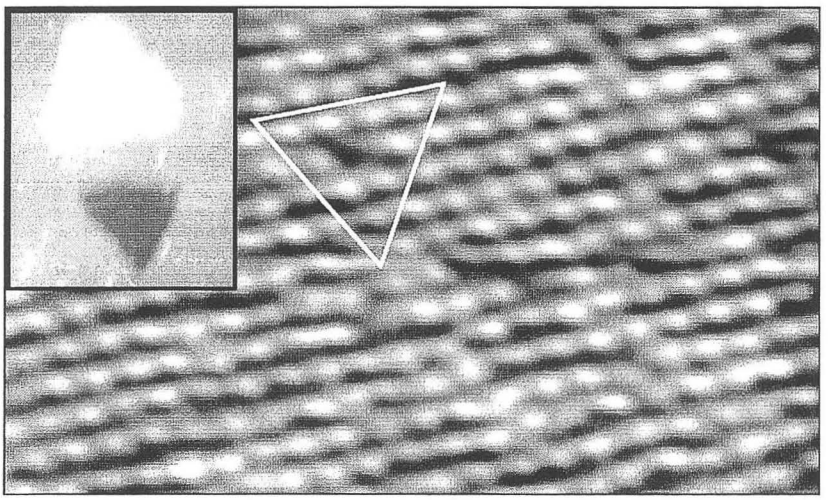

Figure 4.2 A 270 Å × 150 Å topographic STM image obtained in 150 Torr CO and 50 Torr O_2 after annealing at 183°C. V_S = +111 mV, I_T = 0.16 nA. The insert, a 1600 Å × 2000 Å STM image, shows the Moiré patterns alignment to [110] step edges (close-packed row direction).

4.4 Conclusions

These results indicate that the observed hexagonal structures must be due to an ordered, hexagonally close-packed layer of CO that is incommensurate with the Pt(111) substrate, forming a Moiré-type interference pattern in the STM images. This dense overlayer is in equilibrium with the gas phase; its close-packed symmetry is maintained by the high pressure adsorbates. The consistent orientation of the Moiré pattern relative to the platinum lattice indicates that the [110] close-packed rows of the (111)-like CO overlayer and the Pt(111) substrate are parallel. Small changes of density in the CO overlayer that shift, even slightly, the CO-CO distance are considerably amplified in the Moiré periodicity, as is seen in the un-annealed structure. Annealing the overlayer allows the CO to adopt a more uniformed spacing, forming a well ordered overlayer as inferred by the well behaved Moiré pattern. Thus, the observed 11 to 13 Å Moiré periodicity corresponds to an intermolecular separation of 3.7 to 3.5 Å, which corresponds to a CO coverage of 0.63 to 0.57 ML, respectively. Fig. 4.3 shows the relationship between the incommensurate CO layer (3.5 Å spacing) and the Pt(111) lattice (2.77 Å spacing).

The present structure formed at room temperature in equilibrium with the CO gas pressure has no correspondence with those observed in UHV at low temperature in previous studies. All the dense structures that are stabilized at low temperature in vacuum form several domains, which have been observed by LEED. The domains are due to different angular epitaxies with the Pt substrate. The interpretation of the LEED data corresponding to these structures is still controversial, with two models being

debated. One involves formation of incommensurate structures [7]. In the other model, CO occupies only high symmetry top and bridge positions [13, 14]. The latter model is appealing in that it agrees with the observation of two well-defined vibrational bands for the CO stretch mode, which have been assigned to the top and bridge sites. It also explains better the intensity of the superlattice spots in the LEED patterns involving large lateral momentum transfers [15].

In electrochemical cells, where similar high coverages can be achieved by virtue of the surface electric field, an incommensurate CO overlayer with $(\sqrt{19} \times \sqrt{19})$R23.4° periodicity relative to the Pt(111) was observed at 0.67 ML [16]. This structure was imaged by *in situ* STM, which revealed the presence of two hexagonal close-packed domains rotated 23.4° relative to the substrate lattice. The resulting Moiré periodicity is 12.1 Å, in the range of our observed value (12 ± 1 Å). A $(\sqrt{7} \times \sqrt{7})$R19.1° structure with a CO coverage of 0.57 ML was also observed. This structure has essentially the same CO spacing as we infer from our data (3.67 Å), but the close-packed CO layer is rotated relative to the substrate lattice (by 19.1°, in this case). Again, this structure forms multiple rotational domains, which are not observed in the high pressure structure. The presence of water, either coadsorbed or forming an ordered layer above it, appears to be necessary to stabilize these structures [17].

Much more relevant to our work are the vibrational spectroscopy data of CO on Pt(111) at high pressures recently obtained by Su et al. [18] using sum frequency generation (SFG). They find that the intensity of 2100 cm^{-1} mode, which corresponds to the on-top site in the vacuum regime, decreases and then disappears when the CO gas pressure reaches 150 Torr. It is replaced by a broad adsorption band in the range of 2050-1900

cm^{-1}, which results from a distribution of modes. Above 300 Torr, this broad band tails all the way down to 1700 cm^{-1}. These results are very different from both the vacuum and the electrochemical cell environments where two well-defined peaks are always observed: an atop site in the 2050-2100 cm^{-1} region, and either a bridge site in the 1850 cm^{-1} region (up to 0.67 ML) or a three-fold site near 1770 cm^{-1} at the highest coverage of 0.75 ML. A quasi-continuous distribution of CO sites that is proposed from these results best fits our model for an incommensurate CO layer.

In conclusion, the novel use of STM in high pressure gas environments has revealed the existence of dense layers of CO on Pt(111) *in equilibrium* with the gas phase at 200-750 Torr at room temperature, forming a new structure that is incommensurate with the underlying Pt(111) lattice and quite different from the structures formed at low temperature in vacuum conditions. It is this structure that is likely to be relevant in catalytic processes that occur only at high pressures [10].

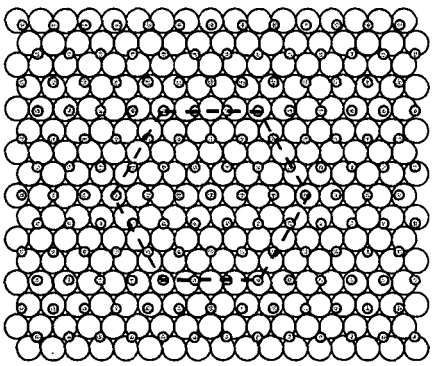

Figure 4.3 Representation of the incommensurate overlayer's relation to the Pt(111) lattice (2.77 Å spacing). Grey circles represent CO molecules (3.5 Å spacing).

1 B.J. McIntyre, M. Salmeron, G.A. Somorjai, *Rev. Sci. Instrum.* **64**, 687 (1993).

2 B. Marchon, P. Bernhardt, M.E. Bussell, G.A. Somorjai, M. Salmeron, W. Siekhaus, *Phys. Rev. Lett.* **60**, 1166 (1988).

3 B.J. McIntyre, M. Salmeron, G.A Somorjai, *J. Vac. Sci. Technol. A* **11**, 1964 (1993).

4 B.J. McIntyre, M. Salmeron, G.A Somorjai, *Science* **265**, 1415 (1994).

5 U. Schröder, B.J. McIntyre, M. Salmeron, G.A. Somorjai, *Surf. Sci.* **331-333**, 337 (1995).

6 H. Steininger, S. Lehwald, H. Ibach, *Surf. Sci.* **123**, 264 (1982).

7 G. Ertl, M. Neumann, K.M. Streit, *Surf. Sci.* **64**, 393 (1977).

8 B. Lang, R. W. Joyner, G. A. Somorjai, *Surf. Sci.* **30,** 454 (1972).

9 D. F. Ogletree, M. A. Van Hove, G. A. Somorjai, *Surf. Sci.* **173,** 351 (1986).

10 J. A. Jensen, K. B. Rider, M. Salmeron, G. A. Somorjai, *Phys. Rev. Let.* **80,** 1228 (1998).

11 The noise level in the STM did not allow us to routinely achieve atomic resolution on the clean Pt(111). Instead, sulfur overlayers forming a (2×2) pattern provided a relatively easy way to determine the substrate orientation since the corrugation is ~0.3-0.5 Å.

12 X.C. Su, P.S. Cremer, Y.R. Shen, G.A. Somorjai, *J. Am. Chem. Soc.* **119**, 3994 (1997).

13 B.E. Hayden, A.M. Bradshaw, *Surf. Sci.* **125**, 787 (1983).

14 B.N.J. Persson, M. Tueshaus, A.M. Bradshaw, *J. Chem. Phys.* **92**, 5034 (1990).

15 D.F. Ogletree, M.A. Van Hove, G.A. Somorjai, *Surf. Sci.* **173**, 351 (1986).

16 I. Villegas, M.J. Weaver, *J. Chem. Phys.* **101**, 1648 (1994).

17 K. Yoshimi, M-B. Song, M. Ito, *Surf. Sci.* **368**, 389 (1996).

18 X.C. Su, P.S. Cremer, Y.R. Shen, G.A. Somorjai, *Phys. Rev. Lett.* **77**, 3858 (1996).

5 Pt(111) in O_2

We performed the experiments in this chapter as a preliminary exercise before studying the CO + O_2 reaction. They were substantially more difficult than the CO experiments described in the previous chapter because tungsten tips are not stable in oxidizing environments, so we were forced to use less robust gold tips. This led us to explore several tip materials and we finally settled on gold tips. We found that preparing sharp gold tips was easy enough, but they rarely stayed sharp because gold is so soft. As a result, it was more difficult to achieve high lateral resolution in oxygen than it was in carbon monoxide. We did find, however, that the Pt(111) surface morphology was significantly different after the crystal was heated in oxygen. We believe that the oxygen adatoms that were adsorbed on the step edges lowered their energy, which caused the surface morphology to change.

5.1 Background

The binding of oxygen atoms to step edges is important in heterogeneous catalysis [1], the promotion of layer-by-layer crystal growth [2] and the morphology of catalyst surfaces [3]. In general, step edges have a different reactivity than terrace sites do. Usually, step edges are more reactive due to the lower coordination of the metal atoms.

When oxygen is deposited on platinum at room temperature, it quickly dissociates into oxygen adatoms. At low coverage, oxygen forms a p(2 × 2) structure with the atoms on the three-fold hollow sites, but it forms a (2 × 1) structure at higher coverage [4,5].

Feibelman [6] demonstrated that oxygen adatoms on Pt(111) have a preference for adsorption near step edges and that they have different binding energies on steps with different orientations.

The stable step edges on Pt(111) have two different structures. One consists of (100) microfacets and the other is made up of (111) microfacets; these are often called *A* and *B* steps. Using first-principles calculations, Feibelman found that oxygen adatoms favor fcc-like sites (sites with no platinum atom in the second layer below the adatom) over hcp-like sites by 0.4 eV. This explained the difference in the appearance of the *A* and *B* steps in his STM experiments [6]. When oxygen adatoms bind behind a *B* step, they sit on fcc three-fold hollow sites, but they favor two-fold bridging sites on *A* steps. The binding energy for oxygen is 5.28 eV on the terrace sites, 5.68 eV on the *B* steps and 5.88 eV on the *A* steps.

5.2 Results and conclusions

A Pt(111) crystal without a gross miscut was cleaned using the same technique that was discussed in the previous chapter; it was then imaged in 20 Torr O_2 with a gold tip. At room temperature no changes in the step morphology could be seen; STM images of the surface showed large terraces between smoothly curved step edges, just like in vacuum (Fig. 5.1). After the sample was heated to 473 K for 10 minutes, the sample was cooled to room temperature and imaged in the 20 Torr background of O_2. These images revealed step edges that were no longer smooth but contained sharp turns and kinks (see Fig. 5.2). The sharp turns in the step edges did not form a regular pattern but meandered randomly. The net increase in the number of steps observed was consistent with the

decrease in the free energy of the Pt(111) step edges when covered with adsorbed oxygen. This was the opposite of the effect that we saw when the sample was heated in vacuum.

No ordered adsorbate structures were visible under these conditions for reasons that are not yet entirely clear. The vertical resolution in the images was high enough to see the expected ~0.1 Å corrugation for the (2×1) structure, so the noise level of the microscope was not to blame. It is possible that the oxygen atoms were rapidly diffusing on the surface, but the high coverages we expect under these conditions should have prevented that. The most likely explanation is that the soft gold tips were quickly blunted during use and decreased the horizontal resolution to the point where the adsorbates were not visible.

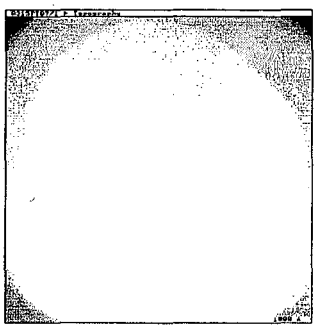

Figure 5.1 STM image of Pt(111) in vacuum. Note the rounded step edges and large terraces. No changes are seen when the sample is held at room temperature in high pressure oxygen.

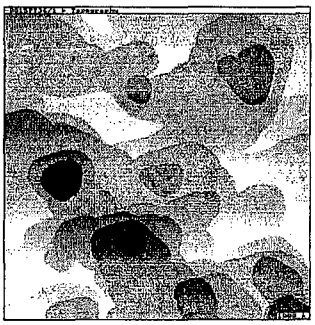

Figure 5.2 STM image taken in an oxidizing atmosphere. A Pt(111) crystal was heated to 473 K for 10 minutes in 20 Torr O_2, then imaged at room temperature. Comparison between images taken before and after heating in O_2 show a dramatic increase in the length of the step edges. Under these conditions W tips are unstable, so Au tips are used.

1 E. G. See, J. Xu, J. T. Yates, Jr., J. Chem. Phys. **99,** 725 (1993)

2 S. Esch, M. Hohage, T. Michely, G. Comsa, Phys. Rev. Lett. **27,** 518 (1994)

3 E. Hahn, H. Schief. V. Marsico, A. Fricke, K. Kern, Phys. Rev. Lett. **72,** 3378 (1994)

4 J. L. Gland V. N. Krochak, Surf. Sci. **75,** 733 (1978)

5 N. Materer, U. Starke, A. Barbieri, R. Doll, K. Heinz, M. A. Van Hove, G. A. Somorjai, Surf. Sci. **325,** 207 (1995)

6 P. J. Feibelman, S. Esch, T. Michely, Phys. Rev. Lett. **77,** 2257 (1996)

6 Rh(111) in CO

The adsorption of CO on Rh(111) is well studied because of its relevance to the CO + NO reaction, which occurs on rhodium particles in automobile catalytic converters. Even though it is so well studied, the structures that CO forms on Rh(111) still have some surprises. In the following sections we will describe Scanning Tunneling Microscopy (STM) studies of the chemisorption of CO on Rh(111) at room temperature. We will concentrate on the high coverage limit (coverage $\geq$ 0.5 monolayers) because it is more relevant to the high-pressure structures. In all cases, a background pressure of CO was maintained during imaging, but some of the structures described here were found at pressures that are generally considered to be in the vacuum regime. This study was particularly interesting because it covers such a wide pressure range. The structures observed at low pressure (10^{-8} to 10^{-6} Torr) include a (2×1) structure and two $(\sqrt{7} \times \sqrt{7})$ R19° structures, which had not been previously observed. In contrast to the low coverage regime, CO occupies both top and three-fold hollow adsorption sites above 3/7 monolayers. Continuing this trend, the highest coverage structure, (2×2)-3CO, was found to be stable under CO pressures of at least 700 Torr and temperatures up to 80 °C.

6.1 Introduction

The adsorption of carbon monoxide on a noble metal surface is one of the most intensely studied gas-surface reactions. The metal surface/CO system is important in the catalytic production of methanol from methane and the oxidation of CO to CO_2 in automobile catalytic converters. Therefore, it is surprising that the molecular details of the reaction

are still not well understood after considerable effort has been devoted to the study of CO adsorption. This is particularly so in the case of high coverage structures, which are the ones likely to be present under high pressure catalytic conditions.

The first structural results on the adsorption of CO on Rh(111) appeared nearly 30 years ago when Grant and Haas [1] found by Low Energy Electron Diffraction (LEED) that CO formed a (2×2) structure. Thiel *et al.* [2] found two structures with $(\sqrt{3} \times \sqrt{3})R30°$ and (2×2) periodicity at coverages of $\theta = 0.33$ and $\theta = 0.75$ monolayers (ML). A hint of a lower coverage (2×2) structure ($\theta = 0.25$) was also mentioned in their work. Based on kinetic desorption data of CO on Rh(111), Payne *et al.* [3] predicted the existence of several ordered phases. These occurred at coverages of 1/3 and 2/3 ML for the $(\sqrt{3} \times \sqrt{3})R30°$ ordering, at 1/4 and 3/4 ML for two (2×2) phases, and at 1/2 ML for a (2×1) order due to next nearest neighbor interactions. Only a few of these structures have been observed by LEED. The known adsorption structures of CO on Rh(111) are summarized in Table 6.1.

Surface structure	Coverage	Adsorption Sites	Reference
(2×2)	0.25	Top	2
$(\sqrt{3} \times \sqrt{3})$R30°	0.33	Top	2, 4, 5, 6
$(\sqrt{7} \times \sqrt{7})$R19°	0.43	Hollow	15
(2×1)	0.5	Top	15
$(\sqrt{7} \times \sqrt{7})$R19°	0.57	Top, Hollow	15
(2×2)	0.75	Top, Hollow	14, 1, 5, 7,, 6, 8
$(\sqrt{3} \times 7)$rect			9

Table 6.1 The known adsorption structures of CO on Rh(111)

Concerning the adsorption site, high resolution electron energy loss spectroscopy studies [10] of the CO vibrations point to top site adsorption for the 0.33 ML structure, as the peak intensity from the CO stretch appears at 2070 cm^{-1}. This assignment was confirmed by Koestner *et al.* [11] using LEED. Top-site adsorption was also proposed by Beutler *et al.* [12] for the 0.33 ML structure and for the lower coverage (2×2) structure based on high-resolution core level photoemission studies.

Using extended Huckel methods with corrections for electrostatic core repulsion, deKoster *et al.* [13] predicted that the most favorable site for CO absorption on Rh(111) was the 3-fold hcp hollow site, which appears to be contrary to the experimental evidence. Hollow site adsorption, however, does occur in the dense (2×2) structure at 0.75 ML. Both fcc and hcp 3-fold hollow sites, in addition to the top site, were found to be occupied in a recent automated tensor LEED analysis by Gierer *et al.* [14]

6.2 Background

6.2.1 (2×1) structure

Cernota *et al.* [15] found that exposing the Rh surface to 5×10^{-8} Torr of CO results in the formation of a LEED pattern of either (2×2) symmetry or three domains of (2×1) symmetry. STM images obtained while maintaining the same background pressure of CO indicate that it is the (2×1) structure that formed. Images of the surface covered with this structure are shown in Fig. 6.1a. Because of the reduced symmetry of the new structure, three equivalent domains are expected with different orientations relative to the rhodium lattice. Fig. 6.1a shows only one such domain, but other domains with different

orientations were also observed. The top image shows a large area with steps produced by dislocation planes crossing the surface. These straight steps meet at angles of 60° and 120°, as expected from (111)-type planes, which are the easy-slippage planes. Since the steps are aligned along the compact $[1\bar{1}0]$-type directions, they provide a useful internal calibration of the crystal orientation for comparison with the atomic scale images. At higher magnification, the images reveal a (2×1) periodicity with the unit cell sides clearly aligned along the compact rows of Rh atoms. The STM unit cell shows elongated maxima on the long side of the unit cell.

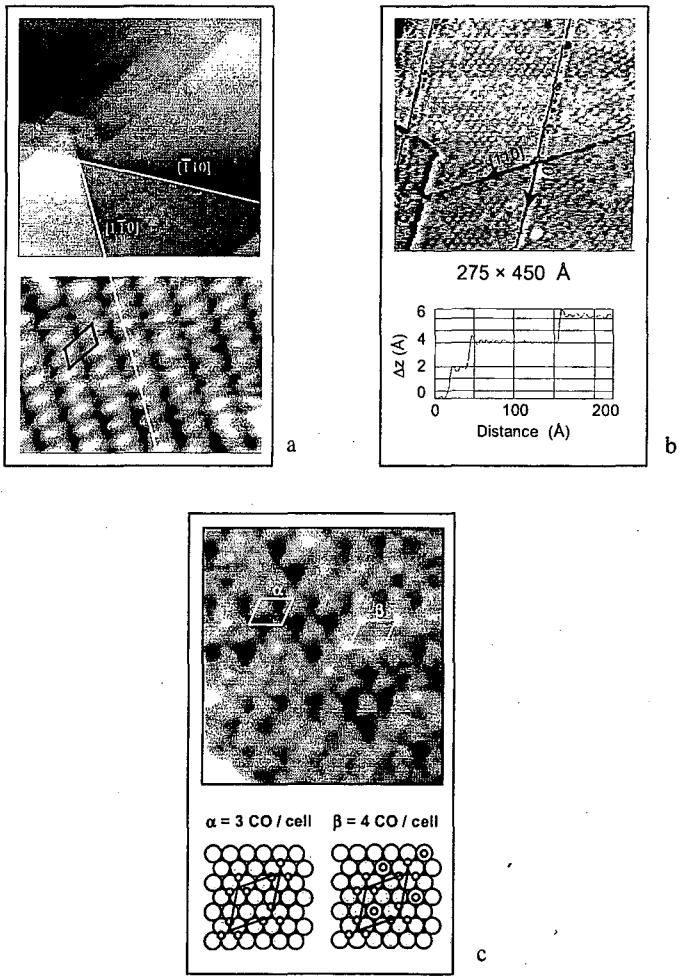

Figure 6.1 High coverage, low pressure structures of CO on Rh(111). (a) Image showing the (2 × 1) structure of adsorbed CO at 5 × 10^{-8} Torr. (b) Image showing the ($\sqrt{7} \times \sqrt{7}$)R19° structure of adsorbed CO at 10^{-6} Torr. (c) Detailed view of the ($\sqrt{7} \times \sqrt{7}$)R19° structure. All of the CO molecules are on hollow-sites (α) at 10^{-6} Torr, but some CO adsorbs on top-sites (β) at 10^{-5} Torr.

6.2.2 ($\sqrt{7} \times \sqrt{7}$) *R19° structure*

Cernota *et al.* [15] also found that, by exposing a rhodum substrate to CO pressures above 10^{-7} Torr, new structures could be observed that had not been reported before. At 10^{-6} Torr, the STM images revealed a periodicity of ($\sqrt{7} \times \sqrt{7}$)R19°. Since the rhodium lattice could not be imaged simultaneously, the assignment was done based on the size of the unit cell and the angles between its unit cell vectors. These angles were accurately calibrated using the angles between [1$\bar{1}$0]-type steps in the same image as a reference. As can be seen in Fig. 6.1b, this angle is 19°. Domains rotated by the expected 21° relative to each other are also observed. These can be seen in the two large upper terraces of the figure or coexisting in the same terrace at the bottom right of the figure. The topographic contrast in the STM images is a few tenths of an Angstrom, as shown in the cursor profile at the bottom of the figure. In these relatively large images, each unit cell appears to exhibit a single maximum. At higher resolution (see Fig. 6.1c), the maxima actually consist of three closely spaced maxima separated by 2.5 ± 0.4 Å (*i.e.,* close to the Rh-Rh nearest neighbor distance of 2.69 Å). They probably correspond to three CO molecules sitting in three neighboring rhodium sites in a triangular arrangement. Such close CO-CO separation also occurs in the dense (2 × 2) structure formed at 0.75 ML, which is described below. The coverage of CO in this trimer structure would be 3/7 (= 0.43 ML), slightly below the 0.5 of the previous (2 × 1) structure, if it occupied the entire surface. The average coverage is higher since additional CO molecules were always seen

between the trimers, producing a strong maximum in the images. These are the brighter spots in Fig. 6.1c.

The CO molecules producing the strong maximum became more numerous as the background CO pressure was increased. At the same time, the size of the unit cell remains identical to the $(\sqrt{7} \times \sqrt{7})$R19°. The fine structure inside the unit cell, *i.e.*, the trimer of weaker spots, became practically invisible when the extra CO was present. This is due to the larger tunneling probability over this site, which causes the feedback control to move the tip away from the surface and results in the loss of detail inside the unit cell. In the example shown in Fig. 6.1c, obtained at about 10^{-5} Torr, nearly 50% of the cells contain the bright spot, which is attributed to the additional CO molecules.

The coverage of the $(\sqrt{7} \times \sqrt{7})$R19° structures varies between 3/7 and 4/7 ML ($0.43 < \theta < 0.57$), depending on the number of bright spots. It is somewhat surprising that the coverage is, at most, only slightly larger than the 0.5 ML from the previous (2×1) structure, considering that the CO pressure is now two orders of magnitude higher. The reason is probably due to the fact that the equilibrium with the gas phase CO can be strongly influenced by small temperature differences of the sample in different experiments. Indeed, 300 K lies in the tail of the thermal desorption peak of CO. To go substantially beyond $\theta = 0.5$ at this temperature, a much larger pressure increase is necessary.

6.3 Experimental

The high-pressure (Torr to atmosphere) STM experiments were carried out in an instrument consisting of two connected chambers separated by a gate valve. One

chamber is a standard UHV chamber, and it is used for preparation and characterization. The other contains an RHK STM scanner and can be pressurized after transferring the sample and closing a gate valve. Details of the design have been published elsewhere [16]. The Rh(111) used in these experiments was cleaned in the most common way: using Ar^+ ion sputtering (500 eV for 15 minutes), oxygen treatment and vacuum annealing (800 °C for 3 minutes). Large-scale STM images of this sample show large (111) terraces with step edges that do not run in a preferred direction on the surface. This indicates that there is no gross miscut angle relative to the (111) surface.

6.4 High pressure (2 × 2)-3CO structure

By increasing the CO pressure up to 0.01 Torr, another structure can be seen by STM. At room temperature and at CO pressures between 0.01 and 700 Torr, a hexagonal pattern is seen with a period of 5.0 ± 0.3 Å. Fig. 6.2 shows an STM image taken in 700 Torr of CO at room temperature, although the structure is stable up to 80 °C. The corrugation in this image is 0.20 ± 0.04 Å. At low temperature, CO is known to form a (2 × 2) structure [14] with a coverage of 0.75 ML. A recent LEED analysis by Gierer *et al.* [8] revealed that the unit cell contains 3 CO molecules: a top-site one and two others in 3-fold hollow sites. It is likely that our (2 × 2) high-pressure structure similarly contains 3 CO molecules.

As can be seen in the image, only one bright spot is visible per unit cell. We assign this spot to the position of the top site CO molecule because it is closer to the tip and, therefore, dominates the tunneling current. The assignment is based on a recent STM image simulation that explains the very similar structure formed by CO on Pd(111) at low

temperature. This calculation indicates that the tunneling probability is much larger at the position of the top CO site, making the other 2 CO molecules in the fcc and hcp hollows sites invisible [17].

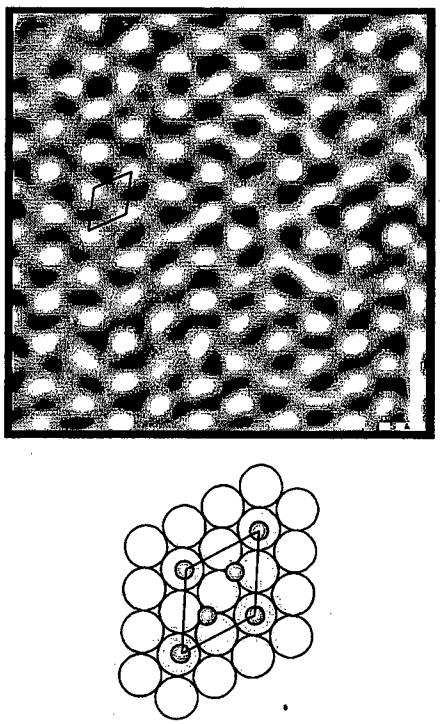

Figure 6.2 A 50 × 50 Å topographic image of the Rh(111) surface in 700 Torr CO. This image shows the (2 × 2) pattern observed in the CO pressure range between 5 and 700 Torr. The average corrugation is 0.20 +/- 0.03 Å.

6.5 Summary and conclusions

Some of the surface science techniques probe ordered surface structures almost exclusively at low pressures (LEED) while others are sensitive to surface bonding regardless of order (vibrational spectroscopy). LEED is not sensitive to small domains of adsorbates, while assignments of adsorbate location from vibrational spectroscopy data can often be ambiguous. STM studies of adsorbate surface structure can be carried out over a 14-orders-of-magnitude pressure range; the surface structure can be obtained in equilibrium with the gas phase; both disordered and ordered phases are detectable. As a result, we have been able to detect dense surface structures formed in equilibrium with gas phase CO on Rh(111) at room temperature. In the past, dense structures could only be analyzed with surface sensitive techniques in non-equilibrium conditions, which typically required cooling the sample to liquid nitrogen temperatures. Thus, we observed (2×1) and $(\sqrt{7} \times \sqrt{7})$R19° structures at coverages of 0.5 and 0.57, respectively, at pressures between 10^{-8} and 10^{-4} Torr. These structures were not known to exist before. We also observed a (2×2) structure above 0.01 Torr, which we believe is similar to the cryogenically stabilized (2×2) structure.

A (2×1) structure was mentioned by Payne *et al.*, associated with the rise and fall of the isosteric heat of adsorption [3]. According to the order-disorder transition theory of Walker *et al.* [18], the existence of (2×1) and/or $(\sqrt{3} \times \sqrt{3})$R30° structures in hexagonal lattices depends on the ratio, r, of second to first nearest neighbor repulsion between CO molecules. A high value of r (> 0.2) tends to favor the existence of only (2

$\times$ 2) and (2 $\times$ 1) structures, while a small value of r (< 0.2) favors the existence of ($\sqrt{3}$ $\times$ $\sqrt{3}$)R30° structures as well. It is possible that these interactions might be fine-tuned by small changes in the state of the substrate—for example, by the presence of impurities or by the presence of subsurface atoms that buckle the surface slightly, *etc.* It is known, for example, that such buckling can dramatically alter the chemisorption properties of Ru surfaces by altering the electronic density between Rh atoms in the surface plane and below it. Since STM is a local probe, it permits the separate investigation of many structures that might exist in areas of the surface of different electronic structure or mechanical stress. Space averaging techniques, on the other hand, might conceivably miss the existence of many surface structures that might be important in catalysis, crystal growth, *etc.*

The (2 $\times$ 1) structure found in our studies cannot be resolved by simple inspection of the STM images. The fact that the periodicity is (2 $\times$ 1) indicates that the coverage is at least 0.5 ML. The STM images show a single maximum per unit cell elongated along the [1$\bar{1}$0]-type direction. This might be due to electronic effects related to the hybridization of the CO orbitals and the Rh orbitals. It could also be due to CO hopping between the top and neighboring bridge sites in the direction of the elongated shape. Since calculated images of CO on Pt(111) always show a round maximum independent of site [19], it appears that rapid (on the scale of STM imaging) site hopping is a more likely explanation. The specific direction of the hopping seems to be pinned by the step direction delimiting the domains. At this point, however, this explanation should be regarded as still speculative.

The shift from the top adsorption site (lowest coordination) to higher coordination sites (bridge or three-fold), which was hinted at in the previous discussion of the (2×1) structure, is dramatically illustrated in the $(\sqrt{7} \times \sqrt{7})R19°$ structure. This structure is surprising in that the content of the unit cell changes as a function of coverage without changing periodicity. At the low coverage end of the structure, the CO adsorption site is exclusively 3-fold hollow. Then, as we have seen, top sites are populated again as the coverage increases. At saturation, the ratio of 3-fold to top sites is 3:1 for this structure. At the highest coverage of 0.75 ML, this ratio is 2:1.

At present, there is no theoretical model to account for the site shift. We can speculate that the shift might be related to a restructuring of the metal surface. There is evidence from LEED crystallography of an upward shift of the Rh atoms under the CO. In the case of the 0.75 ML (2×2) structure, the first layer of Rh atoms is shifted upwards by about 0.07 Å. Reconstruction is also implicated by SFG studies at high CO pressures; however, there is no evidence for the formation of $Rh(CO)_2$ carbonyls on Rh(111) that were detected by infrared spectroscopy over rhodium particles dispersed on alumina. The possibility of gas phase carbonyls producing this structure can also be ruled out since no such effects were observed at the even higher pressures used to produce the (2×2) structure. Moreover, any carbonyl in the gas phase would have to originate before introduction in the high vacuum chamber, since only then would the CO pressure in the container be high enough. Again, no carbonyl related structures were ever observed in the other surface structures produced with the same gas pressure before the leak valve.

In summary, dense structures of CO on Rh(111), which have coverages of 0.5 ML and above, can be formed at room temperature in the presence of a background pressure gas.

New structures were formed, with (2×1), $(\sqrt{7} \times \sqrt{7})$R19° and (2×2) structures in the pressure range 10^{-8} to 700 Torr, which is nearly 11 orders of magnitude. The coverage only changed from 0.5 to 0.75 ML in this range. A shift in the adsorption site occurs from the favored top site at the coverages of 0.33 and below to pure 3-fold sites in the low coverage version of the $(\sqrt{7} \times \sqrt{7})$R19° structure to mixed 3-fold (fcc and hcp) and top sites in the (2×2) structure. These structures, which exist in equilibrium with gas phase CO, are likely to be the relevant ones in catalytic systems operating in non-UHV conditions.

---

1 J.T. Grant, T. W. Haas, *Surf. Sci.* **21,** 76 (1970).

2 P.A. Thiel, E.D. Williams, J.T. Yates, Jr., W.H. Weinberg, *Surf. Sci.* **84,** 54 (1979).

3 S.H. Payne, H.J. Kreuzer, K.A. Peterlinz, T.J. Curtis, C. Uebing, S.J. Sibener, *Surf. Sci.* **272,** 102 (1992).

4 R. J. Koestner, M. A. Van Hove, G. A. Somorjai, *Surf. Sci.* **107,** 439 (1981).

5 D. G. Castner, B. A. Sexton, G. A. Somorjai, *Surf. Sci.* **71,** 519 (1978).

6 L. A. DeLouise, E. J. White, N. Winograd, *Surf. Sci.* **147,** 252 (1984).

7 P. A. Thiel, E. D. Williams, J. T. Yates, *Surf. Sci,* **84,** 54 (1979).

8 M. A. Van Hove, R. J. Koestner, J. C. Frost, G. A. Somorjai, *Surf. Sci.* **129**, 482 (1983).

9 C. M. Mate, B. E. Bent, G. A. Somorjai, *J. Electron Spectrosc. Rel. Phenom.* **39,** 205 (1986)

10 L.H. Dubois, G.A. Somorjai, *Surf. Sci.* **91,** 514 (1980).

11 R.J. Koestner, M.A. Van Hove, G.A. Somorjai, *Surf. Sci.* **107,** 439 (1981).

12 A. Beutler, E. Lundgren, R. Nyholm, J. N. Andersen, B. Setik, D. Heskett, *Surf. Sci.* **371**, 381 (1997).

13 A. deKoster, R. A. van Santen, *J. Vac. Sci. Technol. A* **6,** 1128 (1988).

14 M. Gierer, A. Barbieri, M.A. Van Hove, G.A. Somorjai, *Surf. Sci.* **391,** 176 (1997).

15 P. Cernota, K. Rider, H. A. Yoon, M. Salmeron, G. Somorjai, *Surf. Sci.* **445,** 249 (2000).

16 J.A. Jensen, K.B. Rider, Y. Chen, M. Salmeron, G.A. Somorjai, *J. Vac. Sci. Technol. B* **17,** 1080 (1999).

17 M. Rose, J.C. Dunphy, S. Behler, D.F. Ogletree, M. Salmeron, Surf. Sci. To be submitted (1999).

18 J.S. Walker, M. Schick, Phys. Rev. B **20,** 2088 (1979).

19 M.L. Bocquet, P. Sautet, *Surf. Sci.* **360,** 128 (1996).

7 Rh(111) in NO

This chapter discusses HPSTM experiments on a rhodium surface in nitric oxide. We discovered that NO formed a new structure on Rh(111) in equilibrium with the gas phase near room temperature and at pressures in the Torr range. Two dense phases formed with (2×2) and (3×3) periodicity. Regardless of whether the boundary was crossed by increasing or decreasing the pressure or temperature, regions of the surface transformed from one phase to the other as the pressure and temperature changed around the equilibrium *P-T* boundary line. By measuring the pressures and temperatures of coexistence, we determined the heat of adsorption of the previously unknown (3×3) structure. We estimated the activation energy barrier between the two phases from the dynamics of the phase boundary line. The results demonstrate that unique information, which expands our understanding of gas-surface interfaces on the atomic scale, can be obtained from high-pressure and high-temperature studies.

7.1 Introduction

Our understanding of the elementary steps of gas-surface reactions comes primarily from experiments performed under low-pressure (10^{-4} – 10^{-10} Torr) conditions, but the motivation for studying many gas-surface reactions is the industrial importance of selective adsorption and heterogeneous catalysis. The difference between traditional low-pressure surface science studies and industrial applications, which are normally carried out at high pressure, is known as the pressure-gap. In addition, the sample temperature during a low-pressure experiment must be very low if the coverage is to remain the same

as that obtained at high pressures. This means that in the divide between traditional surface science and its industrial motivation, there is not only a pressure-gap but also a concomitant temperature-gap. Bridging these gaps is critical for a fundamental understanding of catalytic phenomena. Although the high surface coverage that prevails in industrial operations at high pressure can be achieved at low pressure by lowering the temperature, the structures formed under the two conditions might not be the same, as we have shown recently in the case of Pt(111) in 200 Torr of CO [1]. At high pressure and temperature, dense structures form in equilibrium with the gas phase, but at low temperature, the structures must be kinetically frozen and not in equilibrium. In addition, the low temperature is likely to prevent the formation of structures that are reached through an activated process, such as surface reconstruction. In our laboratory, these problems have been overcome through the development of a high-pressure, high-temperature scanning tunneling microscope (STM).

Here, we report the discovery of new structures of NO on Rh(111) formed at pressures in the Torr range and their transformation dynamics. Two ordered structures, which were only slightly different in density, were found with (2×2) and (3×3) periodicity relative to the rhodium substrate. Regions of the surface transformed from one structure to the other as the temperature and pressure fluctuated around a phase equilibrium line. The heat of adsorption of molecules in the (3×3) structure was determined using the two-dimensional analog of the Clausius-Clapeyron equation.

The adsorption of NO on Rh(111) in vacuum is well understood, and several ordered structures are known. A LEED and HREELS study [2] found that NO binds in hollow sites at 95 K without lateral order. Adsorption of small amounts of NO at higher

temperatures causes dissociation into N and O adatoms [3]. At 120 K, 0.5 ML of NO forms a c(4×2) structure with all of the molecules sitting on the same adsorption site, presumably the three-fold hollow site, but there is some debate on that issue [4, 5, 6]. At 250 K, 0.75 ML of NO forms a (2×2)-3NO structure with two molecules sitting on hollow sites and one sitting on a top site. The known adsorption structures of NO on Rh(111) are summarized in Table 7.1.

A (2×2) structure with a coverage of 0.75 ML is known to form either by large (~20 Langmuir) exposures to NO at 200 K, or by small (~2 Langmuir) exposures at 40 K, followed by annealing to 200 K. At room temperature, it is possible to maintain this structure with a constant background of 10^{-8} Torr. X-ray photoelectron diffraction [5] and automated tensor LEED [7] studies indicate that the unit cell of this structure contains three NO molecules; one sits on a top site and two sit in three-fold hollow sites. The top-site NO molecule sits 0.4 Å higher than the hollow site molecules.

Surface Structure	**Coverage**	**Adsorption Sites**	**Reference**
(3 × 3) electrochemical	0.44	Top, Bridge	8
c(4 × 2)	0.5	Hollow	9
(2 × 2)	0.75	Top, Hollow	9, 10
(3 × 3) high pressure	0.77	Top, Hollow	10

Table 7.1 The known adsorption structures of NO on Rh(111)

7.2 Experimental

The STM was housed in a reactor chamber, which was connected to a standard ultra-high vacuum surface science apparatus in which the samples were prepared and characterized. After transferring the sample to the reactor chamber, gate valves were closed to isolate the chamber and high-pressure gases were introduced. The capabilities of the instrument are described in detail elsewhere [11,12].

The sample was cleaned by Ar^+ sputtering and by annealing in O_2. Auger spectroscopy revealed that carbon, which is the most common contaminant, made up less than 5% of the surface. After cleaning, the sample was moved to the high-pressure chamber and imaged by STM using etched tungsten tips.

7.3 Results and discussion

In the range of 10^{-8} to 0.01 Torr of NO at room temperature, the images show the same (2 × 2) periodicity, with only one maximum per unit cell. The structure is similar to the one formed by CO on Rh(111) and Pd(111). STM studies of these two structures also show one maximum per unit cell [13]. According to theoretical calculations, that maximum corresponds to the CO molecule in the top site [14]. It is likely that the same is true for the (2 × 2)-3NO structure.

When the pressure is increased at a rate of approximately 0.001 Torr/minute, the adsorbed layer of NO molecules remains in equilibrium with the gas phase. As the pressure enters the range between 0.01 and 0.05 Torr, areas of the surface that are

covered with a (3 × 3) pattern can be seen. These areas grow over the course of a few hours until the entire surface is covered by the (3 × 3) structure. Fig. 7.1 shows a series of 100 Å × 100 Å images that were taken 55 seconds apart on the same area of the surface in 0.03 Torr of NO. In image 1a, the majority of the surface is covered with the (2 × 2) pattern with one corner showing a small area of the (3 × 3) pattern. The boundary line (shown in white) propagates at a rate of about 20 Å/minute from the upper-right corner to the lower-left. In images 1a and 1b, a defect has been marked as a reference.

In Fig. 7.2, we show an island of (3 × 3) structure (inside the dotted line) surrounded by areas with the (2 × 2) structure. Two straight lines have been drawn that separate two unit cells of the (3 × 3) structure or three unit cells of the (2 × 2) structure. The cursor profile along line A-B (shown at the bottom) reveals two interesting differences between these NO structures: the corrugation of the (3 × 3) structure is always higher, and the apparent height is greater in the (3 × 3) regions. In the present image, the corrugation in the (3 × 3) region is 0.2 Å on average, compared with the 0.1 Å corrugation of the (2 × 2) region. As a result of different tunneling conditions and tip structures, these values vary by a factor of two from image to image. On average, the (3 × 3) to (2 × 2) corrugation ratio is 4 to 1. Also, in the same figure, the apparent height of the regions covered by the (3 × 3) structure is ~0.1 Å higher than that of the regions covered by the (2 × 2) structure. In general, this apparent height difference varies between 0.1 and 0.5 Å, again depending on tunneling conditions and tip structure. The higher corrugation of the (3 × 3) structure could be the result of the larger dimensions of the unit cell, which causes the top-site NO molecules to be farther apart and allows the tip to better follow the molecular contours.

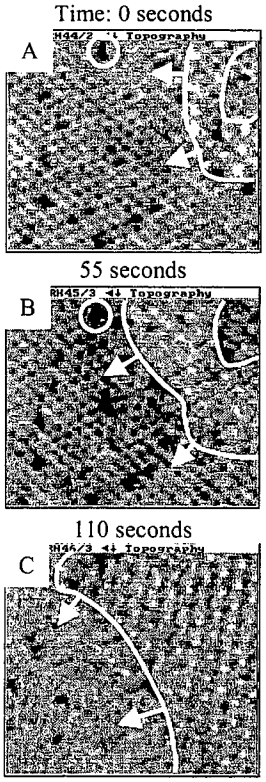

Figure 7.1 STM images of Rh(111) taken in 0.03 Torr of NO at 25°C, showing the phase transition between a (2×2) and a (3×3) structure. The 100 Å × 100 Å images were taken at 55 seconds intervals (I = 440 pA, V = 99 mV). In image a, the majority of the surface shows the (2×2) structure, except for the upper right-hand corner which shows the (3×3) structure. In images b and c, the domain boundary between the two phases moves across the image at a rate of ~20 Å /minute. Images a and b share a common defect, marked with a circle. The close packed rows of both patterns are aligned, and the maxima separated by multiples of the Rh-Rh distance. This indicates that the bright spots correspond to NO molecules on similar sites in both the (2×2) and the (3×3) structure.

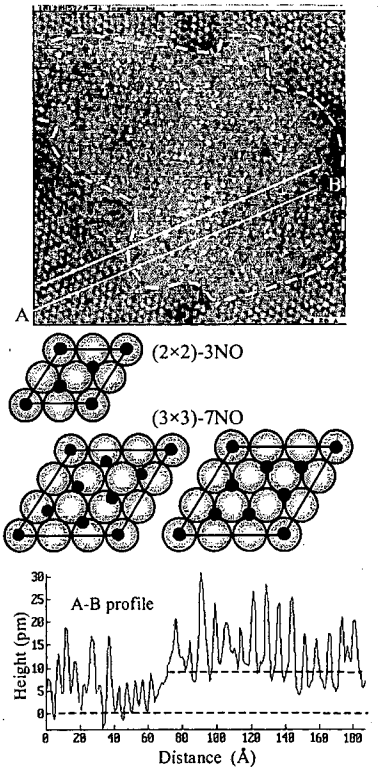

Figure 7.2 A 200 Å × 200 Å STM image taken in 0.03 Torr NO at 25°C, showing a (3×3) domain surrounded by the (2×2) structure. It is known that the (2×2)-3NO structure contains one top-site NO molecule and two molecules on hollow-sites. Two similar models are proposed for the (3×3) structure. The first (left) consists of one top-site NO molecule and 6 molecules near hollow-sites. In the second model (right), the near hollow-site molecules are allowed to relax so that they can occupy 3-fold hollow-sites. Both models have a 0.778 ML coverage and are consistent with the STM images. A line profile taken from line A-B on the image is shown. Note the higher corrugation in the (3×3) domain and its higher apparent height, ~0.1 Å above that of the (2×2) domain.

The corrugation could also be the result of a restructuring of the rhodium substrate. The higher elevation of the base line in the denser structure might indicate an expansion of the top layer of rhodium atoms. The answer to these interesting questions requires experiments with other techniques, such as X-ray diffraction.

Though the (2×2) structure has been solved by LEED, no information is available concerning the (3×3) structure. The models shown in the middle of Fig. 7.2 are proposed based on the following considerations. First, the coverage in the (3×3) structure must be only slightly higher than the coverage of the (2×2) structure (0.75 ML) because the (2×2) structure is already very dense (only 3.16 Å separates adjacent molecules). Second, the STM images show that the rows of maxima in both structures are parallel and are separated by multiples of the Rh-Rh distance. This indicates that the NO molecules producing the maxima occupy similar on-top sites in both structures. A (3×3) structure satisfying these two conditions and preserving the hexagonal packing of NO found in the (2×2)-3NO can be obtained by a rigid rotation of the NO layer by 10.9° followed by a linear compression of 1.8%. A more symmetric structure with NO molecules in 3-fold hollow sites can be obtained by allowing a small relaxation of the NO molecules inside the cell. In both of these models, the surface coverage is 0.778 ML, which is only 3.7% larger than the (2×2)-3NO coverage.

Another interesting observation is the facile displacement of the boundary between the two NO structures. These fluctuations of the boundary are indicative of a dynamic equilibrium between the gas and surface. Fig. 7.3 illustrates this phenomenon more dramatically. A series of 500 Å × 500 Å images were taken at a constant pressure of 0.01

Torr. Although the large size of these images does not allow the individual cells to be visible, high-resolution images show that the bright areas are domains of the (3×3) structure and that the dark areas are domains of the (2×2) structure. In image a, several (3×3) domains can be seen, labeled 1, 2 and 3. Initially, domains 1 and 2 are part of a larger domain. In images b-e, this domain splits in half and domain 1 dissipates. In image f, domains 1 and 2 have dissipated, but domain 3 remains. In the next image (which is not shown), domain 3 has also dissipated, leaving a surface entirely covered by the (2×2) structure. The formation of the (3×3) domains does not appear to be affected by the presence of the tip, since similar phenomena are observed whether the gas is added with the tip far from the surface or within tunneling range. The facile displacement of the boundary between the two structures, which occurs in a time scale of seconds, indicates that they are energetically separated by a barrier of approximately 0.7 eV [15], which allows thermal fluctuations to convert small areas of the surface from one structure to the other. This barrier, of course, is not the energy difference between the two structures, as we discuss next.

Until now, we have described experiments performed at room temperature. To study the phase equilibrium and the energy difference between the two structures, experiments were performed at temperatures between 300 K and 350 K. As expected, the phase transition pressure P increases as a function of temperature T. Fig. 7.4 is a plot of $\ln(P)$ vs. $1/T$, where each point represents a pressure and temperature in which both (2×2) and (3×3) structures were observed on the surface. In the region close to the line, both structures are visible, even after long periods of time (more than 12 hours).

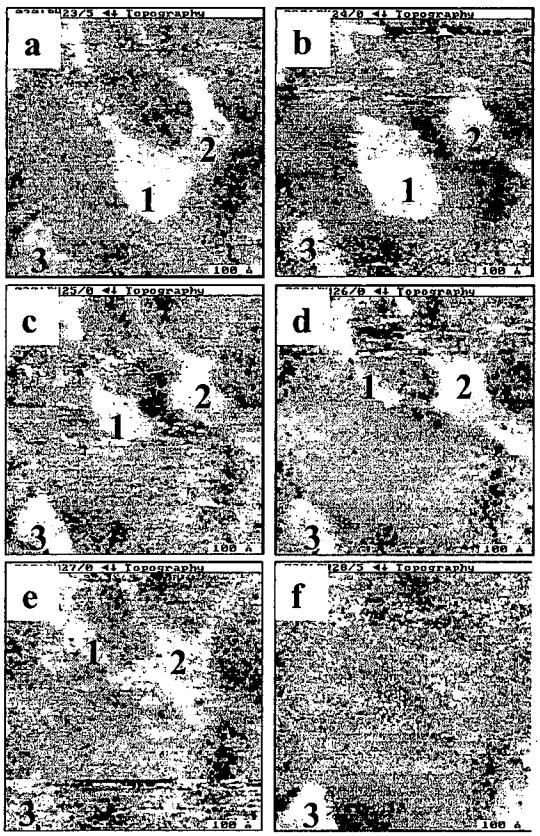

Figure 7.3 A sequence of 500 Å × 500 Å STM images taken in 0.01 Torr NO at 25°C, showing the evolution of a domain of the (3×3) structure (I = 214 pA, V = 101 mV). The brighter area is the (3×3) structure and the darker background is the (2×2) structure. The images were taken 55 seconds apart. In image a, several (3×3) domains can be seen, labeled 1, 2 and 3. Initially 1 and 2 are part of a larger domain. In images b-e, this domain splits in half and domain 1 dissipates. In image f, 1 and 2 have dissipated, but 3 remains. In the next image, domain 3 has also dissipated, leaving a surface entirely covered by the (2×2) structure (not shown).

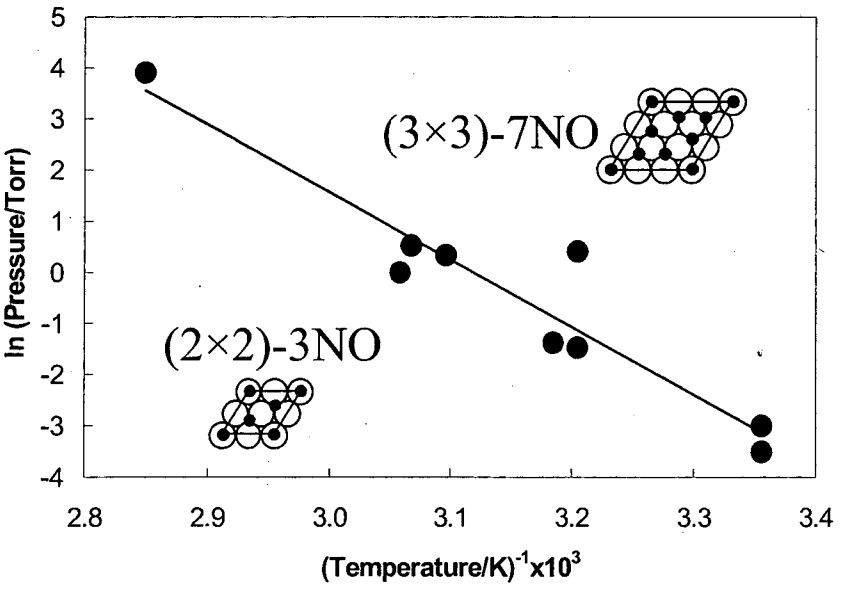

Figure 7.4 Plot of ln(P) vs. $1/T$ for values where the (2×2) to (3×3) transition takes place. The line through the experimental points (•) separates regions where the (2×2) structure is stable (below) and where the (3×3) structure is stable (above). The slope of this line is 1.1 ± 0.2 eV/k.

In the region above the line, only the (3 × 3) structure is observed; below the line only the (2 × 2) structure is observed. The slope of the straight line is 1.1 ± 0.2 eV/k (k = Boltzman constant). The relation between this slope and the heats of adsorption is discussed below.

The state of the gas-surface system is described by three variables P, T and φ, where φ is the two-dimensional surface pressure. When the system consists of a gas phase and two surface phases (1 and 2, for the (2 × 2) and (3 × 3) phases, respectively), the equilibrium condition $\mu(P,T) = \mu_1(P,T,\varphi) = \mu_2(P,T,\varphi)$ places two constraints on P, T and φ, leaving one degree of freedom. It is this degree of freedom that is represented by the line in Fig 7.4. According to Hill [16], when a perfect gas is in equilibrium with two surface phases

$$\frac{d\ln P}{dT} = \frac{\Gamma_2(H_2 - H_g) - \Gamma_1(H_1 - H_g)}{kT^2(\Gamma_1 - \Gamma_2)},$$

where H_i is the molar enthalpy of phase i and the Γ_i terms are the coverages for the surface phases. Recognizing that $(H_1\text{-}H_g)$ and $(H_2\text{-}H_g)$ are heats of adsorption, which we will call h_1 and h_2,

$$\frac{d\ln P}{d(1/T)} = \frac{\frac{\Gamma_1}{\Gamma_2}h_1 - h_2}{k(\Gamma_1/\Gamma_2 - 1)}.$$

The heat of adsorption for Rh(111) surfaces saturated with NO in low-pressure conditions has been measured to be 1.0 ± 0.1 eV [6]. Under these conditions, the surface forms the (2 × 2)-3NO structure, so h_1 = 1.0 eV. From the slope in Fig 7.4 and given that Γ_2 = 0.778 and Γ_1 = 0.75, we calculate the heat of adsorption for the (3 × 3)-7NO structure to

be 0.9 ± 0.1 eV. The difference in the heat of adsorption for the two structures is therefore of order 0.1 eV, a result anticipated from the observation that the two phases can occupy similar areas of the surface.

7.4 Summary

The novel observation of molecularly resolved surface phenomena at high pressure and temperature heralds the beginning of a new era in surface science. By bridging the pressure and temperature gaps with high-pressure, high-temperature STM, we have the opportunity to study molecular level structures and processes at gas-surface interfaces under conditions that were previously inaccessible. We have shown that NO undergoes a phase transition from the (2 × 2)-3NO structure, which is known from low-pressure surface science experiments, to a new (3 × 3) structure, which only forms in equilibrium with the gas phase at high pressure. By directly observing the transition between these structures at several temperatures and pressures, we could measure the heat of adsorption in the new structure to be 0.9 ± 0.1 eV, and from the dynamic behavior of the phase boundary, we deduced an energy barrier of approximately 0.7 eV. It is clear that these are the types of studies that are most relevant to a molecular level understanding of surface catalyzed reactions.

---

1 J. A. Jensen, K. B. Rider, M. Salmeron, G. A. Somorjai, *Phys. Rev. Let.* **80,** 1228 (1998).

2 T. W. Root, L. D. Schmidt, G. B. Fisher, *Surf. Sci.* **134,** 83 (1983).

3 T. W. Root, G. B. Fisher, L. D. Schmidt, *J. Chem. Phys.* **85,** 4679 (1986).

4 K. Christmann, Introduction to Surface Physical Chemistry, Springer-Verlag, New York, (1991).

5 Y. J. Kim, S. Thevuthasan, G. S. Herman, C. H. F. Peden, S. A. Chambers, D. N. Belton, H. Permana, *Surf. Sci.* **359,** 269 (1996).

6 H. J. Borg, J. F. C.-J. M. Reijerse, R. A. van Santen, J. W. Niemantsverdriet, *J. Chem. Phys.* **101,** 10052 (1994)

7 I. Zasada, M. A. Van Hove and G. A. Somorjai, *Surf. Sci.* **418,** L89 (1998).

8 Ze-Haw Zang, Zi-Lin Wu, Shueh-Lin Yau, *Langmuir* **15,** 8750 (1999)

9 D. G. Castner, B. A. Sexton, G. A. Somorjai, Surf. Sci. **71,** 519 (1978).

10 K. B. Rider, K. Hwang, M. Salmeron, G. A. Somorjai, *Phys. Rev. Let.* **86,** 4330 (2001)

11 J. A. Jensen, K. B. Rider, Y. Chen, M. Salmeron, G. A. Somorjai, *Journal of Vacuum Science & Technology B* **17**, 1080 (1999).

12 B. J. McIntyre, M. Salmeron, G. A. Somorjai, *Rev. Sci, Instrum.* **64,** 687 (1993).

13 M. Rose, M. Salmeron, unpublished data

14 M. Rose, M. Salmeron, P. Sautet, unpublished data

15 This energy barrier is estimated using $t\ (1\ sec) = \tau.exp(E/kT)$, with $\tau = 10^{-13}$ sec. A change of this value by an order of magnitude changes the value of E by 7%.

16 T. L. Hill, *J. Chem. Phys.* **17**, 520 (1949)

8 Rh(111) in CO + NO

The high pressure coadsorption of NO and CO on Rh(111) is the logical next step after the work described in the previous two chapters. This chapter describes STM experiments done on the Rh(111) surface in equilibrium with NO + CO gas mixtures. For low NO partial pressures, the NO molecules mix into the CO (2×2)-3CO structure, substituting for the CO molecules without changing the symmetry of the adsorbate layer. As the NO partial pressure increases, the number of top-site NO molecules visible by STM increases. There appears to be a slight preference for NO molecules to sit on adjacent top sites in the (2×2) lattice; this preference causes the formation of NO-rich islands at higher NO partial pressures. The presence of CO in the gas phase prevents the formation of the NO (3×3) structure until the NO partial pressure is three to five times greater than the CO partial pressure. When the (3×3) structure forms, it nucleates on the NO-rich areas mentioned above.

8.1 Introduction

The interaction between CO and NO on Rh(111) is of considerable interest because of its importance in the reduction of NO in automobile catalytic converters. Modern engines produce exhaust in which the combined CO + NO partial pressure is approximately 5 Torr. As the exhaust flows through the catalytic converter, rhodium particles are responsible for catalyzing the reaction of CO + NO to form N_2 and CO_2. Several kinetic models have been proposed [1, 2, 3, 4, 5, 6, 7, 8, 9, 10, 11, 12] for the mechanism, but nearly all agree (5 and 6 are exceptions) that the initial steps are the adsorption of CO and

NO, then the dissociation of NO. Many reaction studies, both in UHV and ambient pressures, have been performed in an effort to understand this reaction [13], but there is little microscopic information about the structure and molecular interactions of the adsorbate layers that form under realistic pressure conditions.

In previous publications, we discussed the structures that form on Rh(111) in CO [14] and NO [15]; now we focus on the coadsorption of these two molecules in the Torr pressure range. This paper discusses the adsorption of NO and CO when they compete for sites on the surface and their binding energies in those sites. It also discusses intermolecular interactions and their effect on the surface structure, namely on the segregation of adsorbates. In addition, we demonstrate that the coadsorption of two molecules can show us more about the motion of molecules on the surface than the adsorption of either molecule independently. Finally, we discuss how CO can prevent the structural phase transition caused by high pressure NO adsorption.

Carbon monoxide adsorbs molecularly at all coverages [16, 17, 18, 19, 20, 21, 22], forming myriad structures due in part to strong CO-CO repulsions [16, 23, 24, 25, 26]. At high coverage, CO forms a (2×2)-3CO structure where the unit cell contains one top-site molecule and two hollow-site molecules [20, 21, 22, 27, 28]. This structure forms at 300 K in UHV and persists until the CO pressure is at least 700 Torr [29]. Temperature programmed desorption (TPD) of CO from this structure shows two peaks, one at 510 K and the other at 430 K, indicating that the binding energy on the two different adsorbtion sites is significantly different. At 1/3 ML, CO binds only to the top site and the three-fold hollow sites are increasingly populated until the surface saturates at ¾ ML, indicating that the top site has a higher binding energy for CO.

The adsorption of NO is more complicated because it dissociates when the temperature is above 200 K and the coverage is below 1/3 ML [18, 30, 31, 32]. Low energy electron diffraction [33, 34] and x-ray photoelectron diffraction [35] have both demonstrated that molecularly adsorbed NO forms a (2×2)-3NO structure at high coverage that is analogous to the CO structure mentioned above. At lower coverage, NO favors the hollow site, as shown by a combination of LEED, XPD, and vibrational spectroscopy (see Permana, et. al. 1 for a discussion of the vibrational peak assignments). The (2×2)-3NO structure exists at 300 K when the surface is in equilibrium with gas phase NO between 10^{-7} and 0.03 Torr; above 0.03 Torr a new structure forms, which has a (3×3) unit cell [15]. One of the objectives of this paper is to explore how the presence of CO affects the formation of the (3×3) structure.

For both NO and CO adsorption, TPD experiments show that the molecules have significantly different binding energies on the top and hollow sites [30, 36], with NO binding more strongly to the hollow site and CO binding more strongly to the top site. There is spectroscopic evidence that the binding preferences of the two molecules are strong enough so that, under reaction conditions, NO binds only to the hollow site and CO binds only to the top site [1, 13]. As we will show later, STM has a very high sensitivity to molecules bound in certain adsorption sites and can therefore identify NO molecules adsorbed on the top sites even when their concentration is just a few parts in a thousand. When CO and NO are coadsorbed on the Rh(111) surface, the spectroscopic evidence indicates that they segregate at low temperature [30] and mix at higher temperatures [1]. Experiments like the ones described in this publication could lead to a detailed understanding of the intermolecular forces that cause adsorbate segregation.

Adsorbate segregation is one of the phenomena that is critically important if we are to find a molecular level model of catalytically active surfaces that correctly predicts macroscopic reaction rates. STM experiments done on systems where there is equilibrium between the surface and the gas phase can indirectly look at intermolecular forces by observing molecular motions and can directly look at surface segregation.

8.2 Experimental

All experiments were carried out in a dual-chamber system, consisting of an ultra-high vacuum chamber attached to a smaller chamber for the STM [37, 38]. The STM, from RHK Technologies, can operate in the 10^{-10} – 10^{3} Torr pressure range and the 300 K – 700 K temperature range. The base pressure of this system was 5×10^{-10} Torr; the background is made up primarily of CO and water without detectable amounts of hydrocarbons.

Our Rh(111) sample was prepared in the vacuum chamber by sputtering with 400 eV oxygen ions for 10 minutes then annealing in vacuum at 973 K for 2 minutes. Just before the sample was exposed to CO or NO, it was flashed briefly to 973 K. The sample temperature was monitored with a chromel-alumel thermocouple mounted in the sample holder so that it was in contact with the edge of the crystal. Our cleaning procedure consistently removed carbon (our only common contaminant) from the surface until the carbon 272 eV Auger peak was no longer visible. The clean, room temperature sample was then transferred in vacuum into the STM chamber. Large scale STM images of the sample showed large (111) terraces with step edges that did not run in a preferred direction on the surface, indicating that there was no gross miscut to the crystal.

When the sample was gong to be imaged in CO or a CO + NO mixture, a leak valve was opened to raise the background pressure to 10^{-7} Torr of CO, then the gate valves were closed, isolating the STM chamber. A constant leak of CO while the chamber was being closed ensured that CO quickly filled the chamber and was always the majority species in the gas phase.

Nitric oxide will dissociate on Rh(111) as long as an ensemble of empty sites is available for the dissociation products, N and O adatoms [13, 18, 30, 31, 32]. The dissociation reaction is inhibited by low temperature (NO does not dissociate at all below 200 K) and high coverage (complete dissociation occurs only below 0.3 ML). Therefore, by prefilling the chamber with CO, NO dissociation could be avoided. In experiments involving both CO and NO, CO was added first then NO to prevent NO dissociation. For experiments involving only NO, the surface was saturated in vacuum as quickly as possible at the lowest temperatures attainable with our system, 243 K, to minimize NO dissociation. Alternatively, we dosed 20 L of CO on the surface at room temperature before transferring the sample to the STM chamber. The two methods did not yield different results.

8.3 Results and discussion

Fig. 8.1a is an STM image of the (2×2)-3CO structure on Rh(111) with the addition of 23% NO. Most of the surface is covered with the low corrugation (2×2) pattern that is characteristic of CO adsorption, but 1% of the top-site positions have bright spots which are 0.3 Å tall. Image 1b shows the surface in a NO/CO gas mixture that is 65% NO; approximately half of the top sites show the 0.3 Å tall bright spots. Since the number of

brighter spots scales with the NO partial pressure, we conclude that these brighter spots indicate the position of top-site NO molecules. Note that no corrugation is seen inside the unit cell, so we cannot distinguish NO from CO on the three-fold hollow sites.

The mole fraction of NO molecules on the top sites is not equal to the mole fraction of NO in the gas phase, but they are roughly proportional. The surface excess of NO on the top sites is

$$\frac{x_{NO,s}}{x_{CO,s}} = \frac{x_{NO,g}}{x_{CO,g}} e^{-\Delta E/kT} \qquad (1),$$

where $x_{NO,s}$, $x_{CO,s}$, $x_{NO,g}$ and $x_{CO,g}$ are the mole fractions of NO and CO on the surface and in the gas phase. The energy, ΔE, in equation (1) is the difference between the differential heats of adsorption for NO and CO on the top sites in the coadsorbed layer.

Fig. 8.2 shows a plot of $1/x_{NO,s}$ vs. $1/x_{NO,g} - 1$, the slope of which is $e^{-\Delta E/kT}$. The slope of the line is Fig. 8.2 has a large uncertainty, but because of the exponential relationship in (1), ΔE is limited to $-(7 +/- 3) \times 10^{-2}$ eV, where the negative sign indicates that CO binds more strongly than NO to the top sites. This result is qualitatively consistent with TPD results [32, 36], but quantitatively, our measurement gives a 0.1% difference in heat of adsorption while the TPD results give a 26% difference, indicating that there are strong NO-CO lateral interactions.

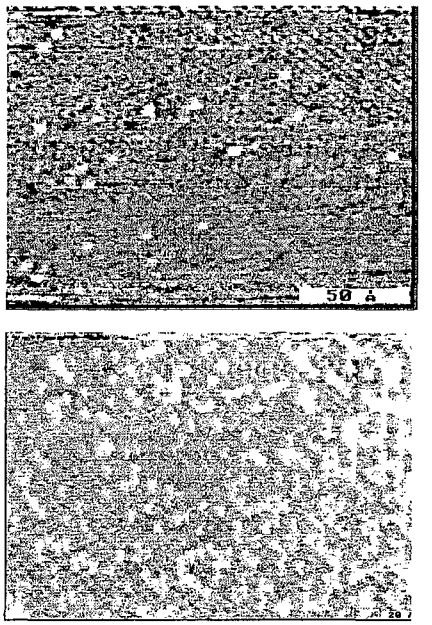

Figure 8.1 STM images taken in a mixture of CO and NO. These 190 Å × 130 Å images display (2×2) pattern with a corrugation of 0.1 Å, which is characteristic of the (2×2)-3CO structure. The brighter unit cells are due to NO adsorption on the top-sites; neither NO nor CO can be seen when it is adsorbed on the hollow-sites. Image 1a was taken in 0.50 Torr CO + 0.15 Torr NO; image 1b was taken in 0.50 Torr CO + 0.70 Torr NO. The CO and NO on the surface appear to be well mixed with the exception of slightly higher NO densities near step edges. This can be seen in image 1b; the right side of the image has a higher NO density than the left side because of its proximity to a step edge. The corrugation of the NO unit cells is 1.5 Å.

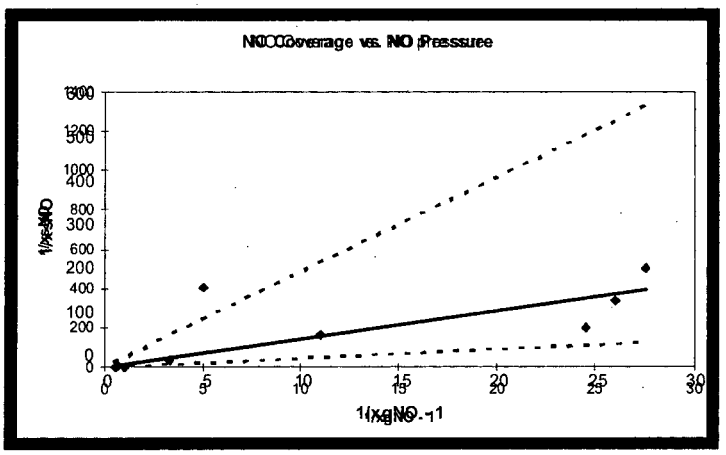

Figure 8.2 Plot of top-site NO coverage vs. NO partial pressure. The mole fraction of NO on the top-sites ($1/x_{sNO}$) was obtained from the images and plotted vs. the mole fraction of NO in the gas phase ($1/x_{gNO}$-1). The slope of the least squares fit line (solid) is $e^{-\Delta E/kT}$, where E is the difference in adsorption energy beween CO and NO on the top-site. We calculate this difference to be $-(7 +/- 3) \times 10^{-2}$ eV, where the uncertainty is estimated by the slopes of the two dashed lines. The negative sign indicates that CO binds more strongly to the top-site than NO.

When the top-site coverage is near 50%, the non-random distribution of the NO molecules is apparent. The STM image in Fig. 8.3 shows how there is a slight preference for NO molecules (brighter unit cells) to have other NO molecules on the neighboring top sites. This suggests one of two plausible explanations: 1) the second nearest-neighbor NO-NO interactions are more favorable than NO-CO interactions, or 2) the adsorption of an NO on a top site enhances the probability of CO adsorption on the nearest-neighbor hollow sites, which, in turn, favors NO adsorption on the second-nearest-neighbor top site. It is interesting to note that this implies that the difference between the NO-NO and NO-CO second-nearest-neighbor interactions is on the order of kT, or 0.025 eV. For comparison, Payne et. al. [25], reports a CO-CO second nearest neighbor interaction of 0.007 eV.

All of the images presented in this article were taken at a scan rate that yields one image every 55 seconds, which raises the question of diffusion on the surface. When the surface is covered with pure CO, as in Ref. 29, each sequential image of the same area appears identical, even as molecules adsorb, desorb and diffuse on the surface. When the surface consists of both NO and CO, however, we can observe any event in which a CO substitutes for an NO or vise versa, at least on the top-site positions. Fig. 8.4 shows a pair of images, taken one after the other, on the same area of the surface. The circles on the images indicate the position of a top-site NO molecule that appears to move one unit cell to the left, indicating that a vacancy has diffused through the two sites. After analyzing ten pairs of images, 64 such events were recorded. The majority of these events (56/64) resulted in an NO molecule moving from one top site to a neighboring top

site one unit cell away, as shown in Fig. 8.4. A much smaller fraction (5/64) resulted in an NO molecule moving two unit cells away, and just 3/64 events resulted in the appearance or disappearance of a top-site NO molecule. Given the fact that any two adjacent top sites are separated by two hollow-site molecules, it does not seem possible that the hopping events are due to an NO molecule moving directly over the hollow sites and into the adjacent top site. It is more probable that the hollow sites are occupied almost exclusively with NO so that when a vacancy moves from the top site to the hollow site, the top site is filled with an NO molecule. Since NO binds preferentially to the hollow site and CO binds preferentially to the top site [32, 36], the most common fate for a top-site vacancy would be for it to be filled with a CO molecule, which explains why the vacancy appears to shift only a small number of molecules before disappearing. To state our model another way, there appears to be a relatively fast exchange of molecules between the top sites and the gas phase CO, a fast exchange between the hollow sites and the gas phase NO, but a relatively slow exchange between the top sites and hollow sites. The adsorption on the hollow sites seems to be dominated by NO, while the CO is disproportionately represented on the top sites.

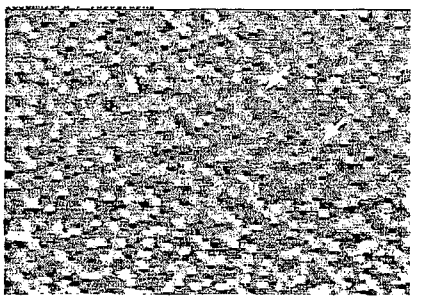

Figure 8.3. STM image taken in 0.50 Torr CO + 0.92 Torr NO. This 190 Å × 130 Å image shows that when the NO top-site coverage is high, the molecules are not randomly distributed. Several places in this image show NO molecules clustering together; for example, between the points marked with arrows there are eight top-site NO molecules next to each other. Two top-site molecules that appear next to each other have two hollow-site molecules between them, so are actually second nearest neighbors. The second nearest neighbor NO-NO interaction must be more favorable than the second nearest neighbor NO-CO interaction.

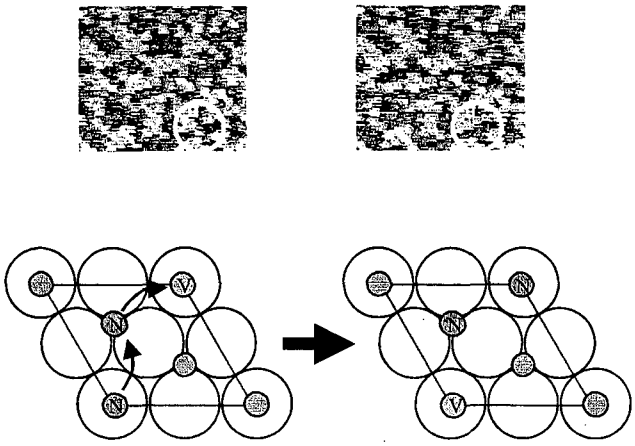

Figure 8.4 Pair of sequential STM images taken 55 seconds apart. These images were taken on the same area of the surface in 0.50 Torr CO and 0.92 Torr NO. In the region marked with a circle, one of the top-site NO molecules appears to move one unit cell toward the top of the image. The diagram shows how a vacancy can diffuse across the unit cell, giving the appearance of a top-site NO molecule hopping from one top-site to another.

When the NO partial pressure is two to four times greater than the CO partial pressure, the relatively favorable NO-NO interaction causes the formation of islands where NO molecules cover all of the top sites. Fig. 8.5 shows two such islands; the (2×2) pattern is visible on the brighter NO covered areas and the darker mixed areas. The typical diameter of one of the NO covered islands is 100-1000 Å. On the microscopic scale, the onset pressure for the formation of the NO islands and the size of the islands do not appear to vary smoothly with the NO partial pressure, although they may do so on larger length scales.

In the absence of CO, NO forms the (2×2)-3NO structure in equilibrium with the gas phase up to 0.03 Torr, then it undergoes a phase transition to a (3×3) structure [15]. Precovering the surface with a monolayer of CO does not modify this behavior, but the presence of CO in the gas mixture does. The images in Fig. 8.6 show the formation of a (3×3) island in the mixed CO + NO layer. In order for the (3×3) structure to form, the NO partial pressure must be three to five times greater than the CO partial pressure. The (3×3) islands first appear as extra bright unit cells in the NO rich areas of the (2×2) layer, as shown in Fig. 8.6a. As the NO pressure is increased, the NO-rich areas nucleate (3×3) islands, as shown in Fig. 8.7b. Interestingly, these brighter spots are positioned over the corners of the (2×2) unit cells, often separated by only one unit cell, or 5.36 Å. In a previous publication [15], we suggested that the large corrugation of the (3×3) structure (compared to the (2×2) structure) may be due to the increased distance between the top-site molecules. These new data show that this is not the case, as the

higher corrugation of the (3×3) structure can first be seen in the (2×2) lattice. The competing hypothesis, as discussed in Ref. 15, is that the corrugation change in the (2×2) to (3×3) transition is due to a reconstruction of the first layer of the metal surface.

The order of introduction of the gases does not affect the final state of the surface, which is to be expected if the gas and surface are in equilibrium. By alternately increasing the NO partial pressure and then CO partial pressure, the surface structure can be changed from (2×2) to (3×3) and back again several times.

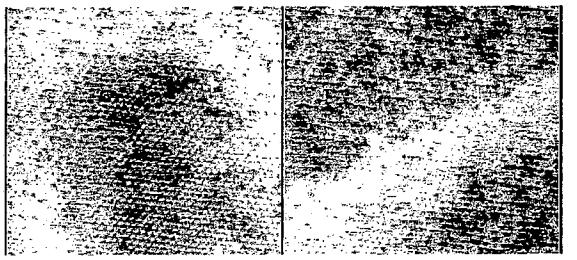

Figure 8.5 STM images showing formation of NO-rich islands. These 200 Å × 200 Å images were taken in 0.10 Torr CO + 0.32 NO. The (2×2) structure is visible with the top-sites being covered with a mixture of CO and NO, but some regions (the lighter areas) have high concentrations of NO on the top-sites.

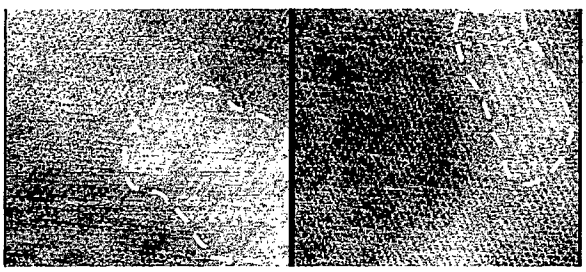

Figure 8.6 STM images showing formation of (3×3) structure. These 200 Å × 200 Å images were taken in 0.10 Torr CO + 0.32 NO. The lighter, NO-rich regions of the surface are the nucleation sites for the formation of the (3×3) structure that is characteristic of high pressure NO adsorption. In the absence of CO, the (2×2) to (3×3) phase transition occurs when the pressure rises above 0.03 Torr.

8.4 Conclusions

The high pressure coadsorption of NO and CO on Rh(111) is a technologically important problem that has a major impact on the operation of automobile catalytic converters. This chapter describes STM experiments done on the Rh(111) surface in equilibrium with NO + CO gas mixtures, where the partial pressures of NO and CO are in the technologically relevant regime. For low NO partial pressures, the NO molecules mix into the CO (2×2)-3CO structure, substituting for the CO molecules without changing the symmetry of the adsorbate layer. NO, like CO, is not visible in the STM images when it is adsorbed on the hollow sites, but it appears as a bright spot with an apparent height of 1.5 Å when it is on the top site. As the NO partial pressure increases, the number of top-site NO molecules visible by STM increases. There appears to be a slight preference for NO molecules to sit on adjacent top sites in the (2×2) lattice, which causes the formation of NO-rich islands at higher NO partial pressures. The presence of CO in the gas phase prevents the formation of the NO (3×3) structure until the NO partial pressure is three to five times greater than the CO partial pressure. When the (3×3) structure forms, it nucleates on the NO-rich areas mentioned above.

A simple statistical analysis of the NO molecule motions in the mixed (2×2) layer indicates that adsorption and desorption of NO onto the top sites is infrequent compared to diffusion within the layer. This analysis also provides indirect evidence that NO molecules predominantly occupy the hollow-site positions.

1 H. Permana, K. Y. S. Ng, C. H. F. Peden, S. J. Schmieg, D. K. Lambert, D. N. Belton, *J. Catal.* **164,** 194 (1996).

2 C. T. Campbell, J. M. White, *Appl. Surf. Sci.* **1,** 347 (1978).

3 L. H. Dubois, P. K. Hansma, G. A. Somorjai, *J. Catal.* **65,** 318 (1980).

4 W. C. Heckler, A. T. Bell, *J. Catal.* **84,** 200 (1983).

5 R. E. Hendershot, R. S. Hansen, *J. Catal.* **98,** 150 (1986).

6 H.-G. Lintz, T. Weisker, *Appl. Surf. Sci.* **24,** 259 (1985).

7 S. B. Schwartz, G. Fisher, L. D. Schmidt, *J. Phys. Chem.* **92,** 389 (1988).

8 C. H. F. Peden, W. D. Goodman, D. S. Blair, P. J. Berlowiz, G. B. Fisher, S. H. Oh, *J. Phys. Chem.* **92,** 1563 (1988).

9 B. K. Cho, B. H. Shanks, J. E. Bailey, *J. Catal.* **115,** 486 (1989).

10 K. Y. S. Ng, D. N. Belton, S. J. Schmieg, G. B. Fisher, *J. Catal.* **146,** 394 (1994).

11 H. F. Peden, D. N. Belton, S. J. Schmieg, *J. Catal.* **155,** 204 (1995).

12 H. Permana, K. Y. S. Ng, H. F. Peden, S. J. Schmieg, D. N. Belton, *J. Phys. Chem.* **99,** 16344 (1995).

13 V. P. Zhdanov, B. Kasemo, *Surf. Sci. Rep.* **29,** 31 (1997).

14 J. A. Jensen, K. B. Rider, M. Salmeron, G. A. Somorjai, *Phys. Rev. Lett.* **80,** 1228 (1998).

15 K. B. Rider, Kevin S. Hwang, M. Salmeron, G. A. Somorjai, *Phys. Rev. Lett.* **86,** 4330 (2001).

16 K. A. Peterlinz, T. J. Curtiss, S. J Sibener, *J. Chem. Phys.* **95,** 6972 (1991).

17 R. J. Koestner, M. A. Van Hove, G. A. Somorjai, *Surf. Sci.* **107,** 439 (1981).

18 D. G. Castner, B. A. Sexton, G. A. Somorjai, *Surf. Sci.* **71,** 519 (1978).

19 P. A. Thiel, E. D. Williams, J. T. Yates, *Surf. Sci.* **84,** 54 (1979).

20 A. Beutler, E. Lundgren, R. Nyholm. J. N. Andersen, B. Setlik, D. Hesket, *Surf. Sci.* **371,** 381 (1997).

21 A. Beutler, E. Lundgren, R. Nyholm. J. N. Andersen, B. Setlik, D. Hesket, *Surf. Sci.* **396,** 117 (1998).

22 M. Gierer, A. Barbieri, M. A. Van Hove, G. A. Somorjai, *Appl. Surf. Sci.* **391,** 176 (1997)

23 D. H. Wei, D. C. Skelton, S. D. Kevan, *Surf. Sci.* **381,** 49 (1997).

24 S. H. Payne, J. Zhang, H. J. Kreuzer, *Surf. Sci.* **264,** 185 (1992).

25 S. H. Payne, H. J. Kreuzer, K. A. Peterlinz. T. J. Curtiss, C. Uebing, S. J. Siebner, *Surf. Sci.* **272,** 102 (1992).

26 L. D. Peterson, S. D. Kevan, *J. Chem. Phys.* **94,** 2281 (1991).

27 M. A. Van Hove, R. J. Koestner, G. A. Somorjai, *Phys. Rev. Lett.* **50,** 903 (1983).

28 M. A. Van Hove, R. J. Koestner, J. C. Frost, G. A. Somorjai, *Surf. Sci.* **129,** 482 (1983).

29 P. Cernota, K. Rider, H. A. Yoon, M. Salmeron, G. Somorjai, *Surf. Sci.* **445,** 249 (2000).

30 T. W. Root, G. B. Fisher, L. D. Schmidt, *J. Chem. Phys.* **85,** 4679 (1986).

31 T. W. Root, L. D. Schmidt, G. B. Fisher, *Surf. Sci.* **134,** 83 (1983).

32 H. J. Borg, J. F. C.-J. M. Reijerse, R. A. van Santent, J. W. Niemantsverdriet, *J. Chem. Phys.* **101,** 10052 (1994).

33 C.-T. Kao, G. S. Blackman, M. A. Van Hove, G. A. Somorjai, C.-M. Chan, *Surf. Sci.* **224,** 77 (1989).

34 I. Zasada, M. A. Van Hove, G. A. Somorjai, *Surf. Sci.* **418,** L89 (1998).

35 Y. J. Kim, S. Thevuthasan, G. S. Herman, C. H. F. Peden, S. A. Chambers, D. N. Belton, H. Permana, *Surf. Sci.* **359,** 269 (1996).

36 T. W. Root, L. D. Schmidt, G. B. Fisher, *Surf. Sci.* **150,** 173 (1985)

37 J. A. Jensen, K. B. Rider, Y. Chen., M. Salmeron, G. A. Somorjai, *J. Vac. Sci. Tech. B* **17,** 1080 (1999).

38 B. J. McIntyre, M. Salmeron, G. A. Somorjai, *Rev. Sci. Inst.* **64,** 687 (1993).

9 Metal Atom Mobility

The previous chapters dealt primarily with the structures of adsorbates on platinum and rhodium surfaces with little mention of the metal itself. This chapter deals with the metal-metal bond and how it is affected by the adsorption of CO or NO.

It is well known that CO and NO change the structure of supported rhodium clusters [1, 2]. In general, they disrupt the Rh particle and form dispersed Rh carbonyls. The strong CO-Rh or NO-Rh bond is responsible for this process; one could think of CO or NO as a surfactant lowering the otherwise very high surface energy of the metal. This chemistry operates only in a certain temperature window–too low and the activated dispersion does not occur, too high and the CO or NO desorbs. Because it requires both high temperature and high coverage, the mobility of metal carbonyls or CO-stabilized metal clusters is only seen at high pressure, so it cannot be studied *in-situ* using ultra high vacuum surface science techniques. STM is able to operate under the temperature and pressure conditions that cause CO-induced metal atom mobility, but it is difficult to use on the small (1 – 10 nm) particles dispersed on high surface area substrates that have been used for infrared absorption experiments. Instead, we work on single crystal model catalysts.

A single crystal, of course, does not disperse to form smaller particles in the presence of CO. The surface metal atoms are still mobile, though, and it is possible that this mobility is responsible for the particle dispersion that is seen in supported catalysts. Single metal atoms on the (111) surface of Pt or Rh are too mobile at room temperature to be observed with STM. We can, however, see the fluctuations in the step-edge shapes, which are a

direct cause of metal atoms moving on the terraces, adsorbing and desorbing from edge sites.

The influence of the STM tip is critically important in studies of metal atom mobility. The STM tip exerts significant forces on the surface atoms, and it is often difficult to determine in a particular instance whether or not the tip is causing the metal atom mobility. When we were faced with this question we realized that, in our experiments, we have never observed metal atom mobility in vacuum or in high pressures of inert gas, even at elevated temperatures. This means that when the metal atom mobility in high pressure reactive gas environments appears to be *affected* by the tip, it is not necessarily *caused* by the tip. In practice, it is not too difficult to see when the tip is affecting the motion of metal atoms on the surface. The STM images by rastering the tip quickly in the left-to-right direction and slowly in the top-to-bottom direction. This creates an anisotropy in the influence that the tip has on the surface; if the metal atoms are being pushed by the tip they tend to move in the left-to-right direction, causing horizontal streaks in the image.

The restructuring of metal surfaces due to the influence of a high pressure reactive gas environment is an interesting and important topic, but it is difficult to study in detail with STM. This is primarily because it is a rare event and one that occurs most often in extremes of temperature and pressure where the microscope is not reliable. The microscope is reliable in the mTorr pressure range at room temperature. As the pressure increases beyond 10 Torr or the temperature increases beyond 500 K, the probability of successful imaging drops to less than 10 %, primarily due to destruction of the STM tip.

The following three sections are examples of the types of step edge mobility that can be seen with STM in high pressure reactive gas environments. It is important to realize that the data in this chapter is fundamentally different than the data in the previous chapters. The previous chapters discussed phenomena that were common and reproducible, where as metal atom mobility is rare and difficult to reproduce.

While the images of Chapters 4-8 were representative samples chosen from a large set of similar images, the images in this chapter are from single events and do not necessarily represent the bulk of the data. Even though the images presented here are from isolated events, there are qualitative similarities between them–similarities that contrast with the low pressure images.

9.1 Pt(111) in CO, room temperature

Consecutive scans revealed the effect of moderate CO pressures on the surface platinum-platinum bonding. Fig. 9.1 shows a series of scans, obtained in 1.0 Torr CO using a tungsten tip, that show mobility of small Pt clusters (≤ 19 atoms). Not only has material been removed from and repositioned along the step edge, but platinum has been removed from the terrace itself, leaving holes and isolated clusters on the (111) plane. These results indicate that chemisorption of a CO molecule onto a surface platinum atom weakens that atom's bonds to the nearest neighboring platinum atoms [3]. Under these experimental conditions of high CO coverage, weak bonding of the surface platinum atoms manifests itself in the easy motion of the platinum atoms in the presence of the tip. Such scan-induced mobility is not observed in UHV or low CO pressures (~ 10^{-6} Torr),

even under more aggressive scanning conditions (i.e., high tunneling current, lower tunneling gap resistance).

The high-CO-pressure-induced softening of the platinum bonds has direct implications to adsorbate-induced metal reconstructions. The weakening of surface platinum bonds by high pressure chemisorbed molecules will enhance diffusion at room temperature, leading to the possibility of restructuring or refaceting the surface at temperatures far below that required in low pressure conditions.

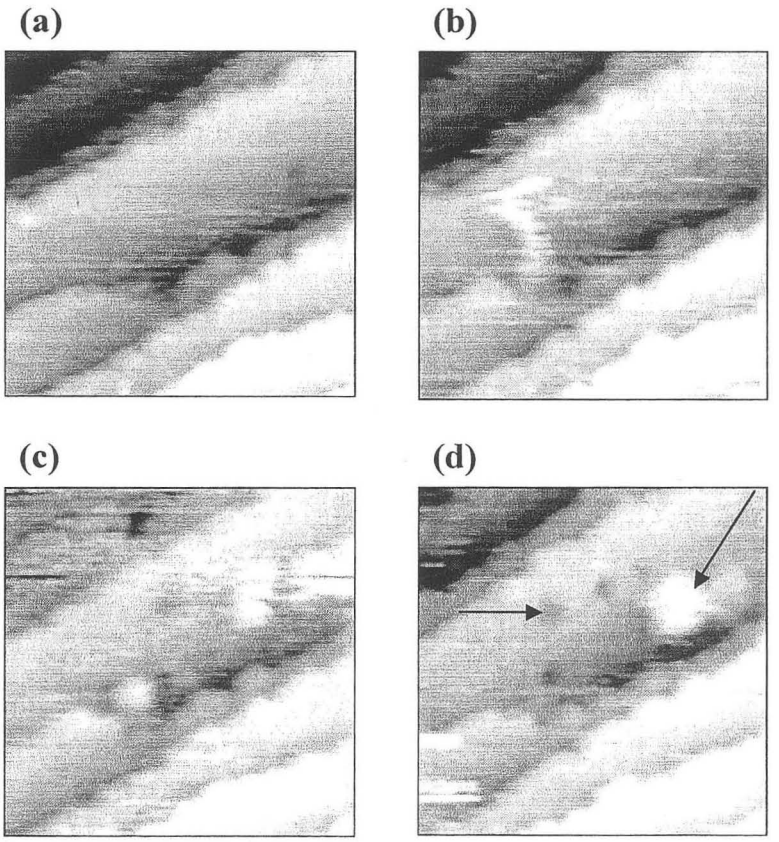

Figure 9.1 Scan induced mobility in 1.0 Torr CO. Pt can be seen to move from the step edges to form islands on the (111) terraces (right arrow). Some Pt is removed from the terraces leaving behind single atom deep holes (left arrow).

9.2 Rh(111) in CO, elevated temperature

To demonstrate the ability of the microscope to work at both high temperature and high pressure, we used a tungsten tip to image a Rh(111) crystal in 20 Torr CO at 323 K. We see the smooth step edges just like in vacuum and CO at room temperature, but we also see the formation of straight step edges that form 60° from each other. Fig. 9.2 shows a series of images taken over a 16 minute period. Initially, two large triangular islands form, then atoms are removed from the apex of one island, while a nearby monatomic hole is filled in. In total, approximately 75 rhodium atoms were removed from the upper terrace to fill in the lower one.

The images of Fig. 9.3 were taken under the same conditions, but on a different area of the surface. They were all taken on the same 4500 Å × 4500 Å area over the course of 10 minutes. Two different types of step edges are apparent: the first type meanders from the top-left corner to the bottom-right corner, the second type is straight and is separated by sharp 60° angles. Vacuum STM images normally only show the first type of step edge. The presence of the high pressure CO clearly favors the straight close-packed step edges that are steadily forming. At lower pressure (10^{-8} Torr) and 323 K, no rhodium mobility is observed, indicating that this effect is caused by high-pressure conditions.

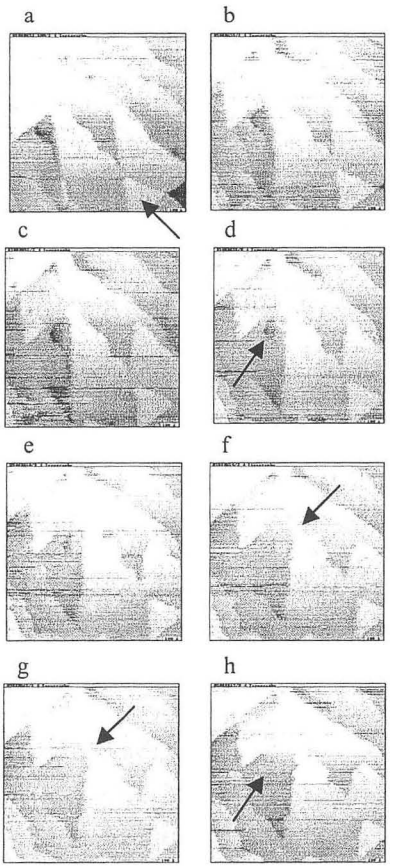

Figure 9.2 Rhodium restructuring in 20 Torr CO at 323 K The images were taken over a 16 minute period. Initially, several triangular islands form (indicated in image [a]), then rhodium is removed from one island as a nearby hole is filled in. The arrows in images [d] and [h] indicated the hole and the terrace formed after it is filled. The arrows in images [f] and [g] indicate the tip of a terrace where atoms are being removed. Each image is 1000 Å × 1000 Å

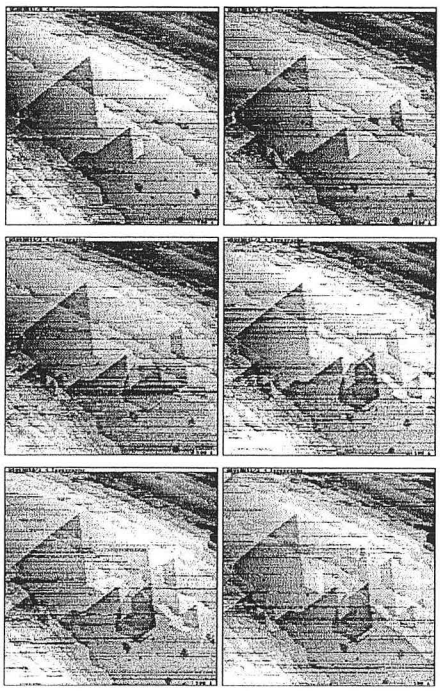

Figure 9.3 STM images taken on the same 4500 Å × 4500 Å area over the course of 10 minutes in 20 Torr CO at 323 K . Two different types of step edges are apparent: the first type meander from the top left corner to the bottom right corner, the second type are straight and are separated by sharp 60° angles

9.3 Rh(111) in CO + NO, room temperature

The most common form of metal atom mobility is the formation of etch pits due to the tip sweeping atoms out of the scan area. Fig. 9.4 shows an example of this type of process at room temperature in 100 Torr CO + 1 Torr NO. First, a horizontal step edge was imaged with the fast scan oriented in the up-and-down direction. This resulted in the vertically oriented etch pits shown in the first image. The subsequent images were taken with the fast scan oriented in the left-to-right direction. The horizontal streaks in the images are due to metal atoms or metal clusters trapped between the tip and surface. Notice that most of the streaks begin at a step edge because it is easier to remove an atom from the step edge than from the terrace itself.

In this case, the motion of the metal atoms is occurring only under the region being scanned and is being caused by a combination of the metal bond weakening and the forces applied by the tip.

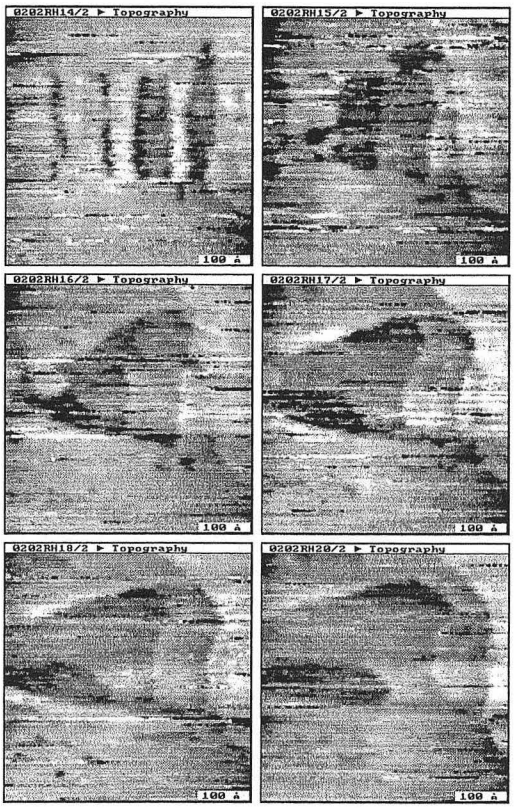

Figure 9.4 Tip induced metal atom mobility at room temperature. These STM images were taken on a Rh(111) surface in 100 Torr CO + 1 Torr NO. The total elapsed time is 7 minutes. The first image shows vertically oriented etch pits, which were caused by quickly moving the tip in the vertical direction. These images are taken with the fast scan direction going from left to right, which quickly removes the material between the etch pits.

9.4 Conclusions

In about 1% of all experiments, we observe motions of the metal atoms. Metal atom mobility is never observed in low pressure ($<10^{-4}$ Torr) CO and is never observed in high pressure inert gas. The surface metal atoms are free to move on the surface only when the CO (or CO + NO) coverage is high and when the temperature is great enough. These two factors explain why this phenomenon is not seen in UHV experiments. Although the tip influences this phenomenon, it does appear that the high pressure reactive gas environment is a critical factor and that the tip is not entirely responsible.

When the tip is moving metal atoms on the surface, it does so by pushing metal atoms off of the step edge sites and occasionally removing a metal atom from the middle of a terrace. As this process continues, the tip etches deeper and deeper into the surface, forming pits. Tip-induced metal atom mobility is the type most commonly observed. Either increasing the pressure or increasing the temperature can induce it, although in most cases the tip fails before the temperature and pressure are high enough for the metal atoms to move. Tip-induced metal atom mobility causes an increase in the number of step sites on the surface, making it more disordered and rough. This is the most common form of metal atom mobility.

In certain instances, the structural changes appear to be driven not by where the metal atoms are removed, but by where they are deposited. When the tip removes a metal atom or cluster from a step edge, it moves over the surface until it finds a suitable step or kink site to deposit on. If the atoms deposit on the first step site they encounter, the result is

rough step edges without any preferred direction. In some cases, it appeared as if the metal atoms were not depositing on the first available step site, but instead they continued to diffuse until a site was available along one of the close-packed rows of the surface. The result is the formation of very straight step edges oriented 60° apart.

We observe an increase in metal atom mobility as the temperature and pressure increase. If this trend continues, as we expect it does, the surface of an active catalyst at a realistic temperature (~700 K) is constantly in motion.

---

1 E. Novak, D. Sprinceana, F. Solymosi, *J. Appl. Catal.* **149,** 89 (1997)

2 P. Basu, D. Panayotov, J. T. Yates, Jr., *J. Am. Chem. Soc.* **110,** 2074 (1988)

3 R. Hoffmann, "Solids and Surfaces," VCH Publishers, New York, (1988).

10 Concluding Remarks

This section summarizes the results and conclusions of the previous chapters and discusses the future of the HPHTSTM project.

10.1 Summary

The primary goals of this research project were to develop the STM as a high pressure technique for use on model catalysts and to apply it to the reactions of the automobile catalytic converter.

An STM was built that has the ability to operate in the 10^{-10} to 10^{3} Torr pressure range (with complete control of the gas environment) and in the 300 – 600 K temperature range. The STM chamber is coupled to an ultra high vacuum chamber so that the sample can be transferred from one to the other without exposure to air. It was found that the most significant difficulty of using an STM in high-pressure reactive gas environments was tip stability. Many tip materials were tested, but only two produced good results : gold tips were found to be useful in CO and O_2 mixtures, but they degraded rapidly, especially at elevated temperatures; tungsten tips were the most useful in CO and CO + NO mixtures.

STM studies of the Pt(111) surface in high pressure CO revealed that CO forms a new structure in the Torr pressure range. The STM images did not reveal the positions of the CO molecules on a molecule-by-molecule basis, but the molecules were imaged via a Moiré pattern. The CO molecules form a close-packed, incommensurate overlayer with neighboring molecules, approximately 3.6 Å apart. The same structure persists up to at

least 750 Torr and is reversible in the sense that the structure disappears when the pressure is reduced to 10^{-4} Torr. This was the first structure determination of an adsorbate in equilibrium with the gas phase at high pressure.

High pressure experiments done on the Pt(111) surface in oxygen revealed changes in the step morphology when the sample was heated. After a platinum sample was heated in oxygen and cooled, STM images showed that the step edges were no longer smooth, as they were before heating, instead they contained sharp turns and kinks. The increase in step edge length was consistent with the previously reported stabilization of step edges due to oxygen adatom adsorption in near-step sites.

The adsorption of carbon monoxide on Rh(111) was studied with a combination of low pressure and high pressure STM experiments. It was found that, contrary to conventional belief, CO does not have a particular adsorption site that is favored at all coverages. When the pressure is less than 10^{-8} Torr the CO coverage is less than 0.5 ML and it favors the top-site. At pressures between 10^{-6} and 10^{-4} Torr CO forms a $(\sqrt{7} \times \sqrt{7})$R19° structure with a coverage that varies between 0.43 and 0.57 ML. At the lower end of this range, the CO molecules are adsorbed entirely on three-fold hollow sites; at the upper end, ¼ of the molecules are on the top sites. When the surface is in equilibrium with CO in the 10^{-3} Torr pressure range, the surface forms a (2×2)-3CO structure with ⅓ of the molecules on the top sites. It has a maximum coverage of 0.75 ML and is stable up to at least 700 Torr.

Nitric oxide binds to the Rh(111) surface in the 10^{-3} Torr pressure range very similarly to CO, forming a (2×2)-3NO structure at a coverage of 0.75 ML. Unlike CO, adsorbed NO undergoes a phase transition to a new structure at approximately 0.03 Torr. The new

structure had never been reported before and would have been difficult to observe with any technique other than STM. Analysis of the STM images revealed that the unit cell of the new structure is (3×3) and there are top-site molecules on the corners of the cell. The corrugation of the new structure was much greater than for the (2×2)-3NO structure and the absolute height was also different, suggesting that perhaps the first layer of the metal surface reconstructs. Both the (2×2)-3NO structure and the (3×3) structure were observed at the same time in the 0.01 – 0.05 Torr pressure range; the domain boundary between the two structures was not static, but fluctuated randomly. The time scale of this fluctuation indicated that the energy barrier along the reaction coordinate for the conversion of one structure to the other is approximately 0.7 eV/molecule. The phase transition pressure was found to increase as a function of temperature. A quantitative analysis of this relationship revealed that the heat of adsorption for the (3×3) structure is 0.9 ± 0.1 eV. The phase transition that forms the (3×3) structure was completely reversible by either decreasing the pressure or increasing the temperature, but this transition only occurs in high-pressure conditions where the surface and gas phase are in equilibrium.

The high pressure coadsorption of NO and CO on Rh(111) was studied using high pressure STM, with partial pressures of NO and CO in the technologically relevant regime. For low NO partial pressures, the NO molecules mix into the CO (2×2)-3CO structure, substituting for the CO molecules without changing the symmetry of the adsorbate layer. As the NO partial pressure increases, the number of top-site NO molecules visible by STM increases. There appears to be a slight preference for NO molecules to sit on adjacent top sites in the (2×2) lattice, which causes the formation of

NO-rich islands at higher NO partial pressures. The presence of CO in the gas phase prevents the formation of the NO (3×3) structure until the NO partial pressure is three to five times greater than the CO partial pressure. When the (3×3) structure forms, it nucleates on the NO-rich areas mentioned above. A simple statistical analysis of the NO molecule motions in the mixed (2×2) layer indicated that adsorption and desorption of NO onto the top sites is infrequent compared to diffusion within the layer. This analysis also provides indirect evidence that NO molecules predominantly occupy the hollow-site positions.

During the course of this research, there were several instances when metal atoms on the surface could be seen in motion, due to the combined effect of the high pressure gas and the STM tip. Chapter 9 presents several case studies of this interesting phenomenon.

10.2 The future of HPHTSTM

There are many interesting directions that this project might take. This thesis demonstrated that HPHTSTM can be used to determine high-pressure adsorbate structures and proved that they cannot be predicted from UHV studies. These findings open up many possibilities for structural studies of other surfaces and adsorbates. Some tentative steps have been made toward examining the dynamics of surfaces under higher temperature conditions; this direction is clearly the most relevant to practical catalytic systems. New tip materials, perhaps carbon nanotubes, will produce tips that are more stable under a wider range of temperatures and in more reactive environments. The results of this thesis are confined to (111) surfaces, which are generally the most stable, other substrates will display a greater tendency to reconstruct and will provide many

fruitful research opportunities. Perhaps the most ambitious line of research will be in the area of supported catalysts—flat, well ordered and conductive oxide films supporting metal nanoparticles could be studied using HPHTSTM, potentially providing insight into spillover and support effects.

Ernest Orlando Lawrence Berkeley National Laboratory
One Cyclotron Road | Berkeley, California 94720

Prepared for the U.S. Department of Energy under Contract No. DE-AC03-76SF00098